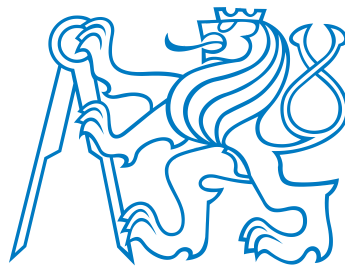


Czech Technical University in Prague
Faculty of Nuclear Sciences and Physical Engineering

Department of Physics



J/ψ Polarization Studies Using the
ATLAS Detector

Master's thesis

Bc. Radek Novotný

Supervisor: prom. fyz. Václav Vrba, CSc.

Consultant: Ing. Michal Marčíšovský, Ph.D.

Prague, 2016

České vysoké učení technické v Praze
Fakulta jaderná a fyzikálně inženýrská

Katedra Fyziky



Studium polarizace J/ψ na
experimentu ATLAS

Diplomová práce

Bc. Radek Novotný

Vedoucí práce: prom. fyz. Václav Vrba, CSc.

Konzultant: Ing. Michal Marčíšovský, Ph.D.

Praha, 2016

Declaration

I hereby declare that this thesis is the result of my own work and all the sources I used are in the list of references.

I have no objection to usage of this work in compliance with the act §60 Law No. 121/2000 Coll. (Copyright Act), and with the rights connected with the copyright act including the changes in the act.

Prohlášení

Prohlašuji, že jsem svou diplomovou práci vypracoval samostatně a použil jsem pouze podklady uvedené v příloženém seznamu.

Nemám závažný důvod proti použití tohoto školního díla ve smyslu §60 Zákona č. 121/2000 Sb., o právu autorském, o právech souvisejících s právem autorským a o změně některých zákonů (autorský zákon).

V Praze dne

.....
Bc. Radek Novotný

Acknowledgement

Foremost, I would like to thank Michal Marčíšovský for his professional guidance, patience, willingness, and invaluable advice. I would also like to thank my supervisor Václav Vrba for overall support of my work and that he provided me the opportunity to participate in this exciting research. Furthermore, I would like to thank Pavel Řezníček for consulting my work and helpful advices and Maria Čarná for her carefully reading of the manuscript. I am also grateful to the classmates for their academic support and for the last five wonderful years spent at the faculty. My greatest gratitude belongs to my family and friends for the continuous support they have given me during my studies. Last but not least I would like to thank my friend Kristýna Vračková for showing me that the beauty of life does not belong only to physics.

Bc. Radek Novotný

Title: J/ψ Polarization Studies Using the ATLAS Detector

Author: Bc. Radek Novotný

Field of study: Nuclear Engineering

Specialization: Experimental Nuclear and Particle Physics

Sort of project: Master's thesis

Supervisor: prom. fyz. Václav Vrba, CSc.

Abstract:

This thesis is devoted to the measurement of the quarkonia properties in proton-proton collisions at $\sqrt{s} = 13$ TeV, using a dimuon data sample recorded by the ATLAS detector at the Large Hadron Collider (LHC). Special attention is given to the measurement of J/ψ polarization which is important for understanding of the production mechanism of heavy quarkonia. The J/ψ polarization parameters λ_θ , λ_ϕ and $\lambda_{\theta\phi}$ are measured in the dimuon decay angular distributions corrected for the reconstruction and trigger efficiencies and kinematic acceptance. The result is obtained in several transverse momentum bins in the range $8 < p_T < 100$ GeV and in the rapidity range of $|y| < 2.0$. Preliminary results, not cleaned of all detector effects, favor isotropic spin alignment of prompt J/ψ .

Key words: J/ψ , quarkonia, ATLAS, LHC, Standard Model, non-prompt production, polarization, spin-alignment

Název práce: **Studium polarizace J/ψ na experimentu ATLAS**

Autor: Bc. Radek Novotný

Obor studia: Jaderné inženýrství

Zaměření: Experimentální Jaderná a Částicová Fyzika

Druh práce: Diplomová práce

Vedoucí práce: prom. fyz. Václav Vrba, CSc.

Abstrakt:

Tato práce je věnována měření vlastností těžkých kvarkonií v proton-protonových srážkách při energii $\sqrt{s} = 13$ TeV využívající data z dimionových událostí měřených na detektoru ATLAS, jenž se nachází na Velkém hadronovém urychlovači (LHC). Zvláštní pozornost je věnována měření polarizace J/ψ mezonu, která je důležitá pro pochopení produkčního mechanismu těžkých kvarkonií. Polarizační parametry λ_θ , λ_ϕ a $\lambda_{\theta\phi}$ jsou měřeny z úhlového rozdělení dimionových událostí, jenž jsou korigovány jak na účinnost triggeru a rekonstrukce, tak na kinematickou akceptanci. Výsledky byly vypočteny v několika binech v transverzální hybnosti v rozmezí $8 < p_T < 100$ GeV a v rapiditě v rozmezí $|y| < 2.0$. Z předběžných výsledků jenž nejsou plně očištěny od detektorových efektů vyplývá, že J/ψ mezon má nulovou polarizaci.

Klíčová slova: J/ψ , kvarkonia, ATLAS, LHC, Standardní Model, nepřímá produkce, polarizace

Contents

1	Introduction	1
2	Theoretical background	2
2.1	Standard model	2
2.1.1	Fundamental interactions	2
2.1.2	Quarks	3
2.1.3	Leptons	4
2.1.4	Antiparticles	4
2.2	Strong interaction	4
2.2.1	Colour	4
2.2.2	QCD	6
2.2.3	Running coupling	7
2.3	J/ψ meson	8
2.3.1	J/ψ polarization	8
2.4	Heavy quarkonia production	11
2.4.1	Color Singlet Model	13
2.4.2	Color Evaporation Model	14
2.4.3	Nonrelativistic QCD Factorization Model	14
2.4.4	k_t -factorization approach	15
2.5	B-physics	17
3	The LHC and ATLAS detector	18
3.1	ATLAS detector	19
3.2	Coordinate system	20
3.3	Magnet system	21
3.4	Inner detector	22
3.4.1	Pixel Detector	22
3.4.2	SCT detector	24
3.4.3	Transition radiation tracker	24
3.5	Calorimetry	25
3.6	Muon spectrometer	26

3.7	Forward detectors	27
4	Data analysis	29
4.1	Data acquisition and processing	29
4.2	Pile-up	30
4.3	Trigger system	31
4.3.1	Trigger menu	32
4.3.2	B-physics trigger	33
4.4	ATLAS software	33
4.5	Monte Carlo simulation	34
4.5.1	Monte Carlo data	35
4.6	Analysis Event Data Model	36
4.7	Event reconstruction	36
4.8	Event selection	37
4.9	Analysis prerequisites	38
4.9.1	Fiducial $J/\psi \rightarrow \mu^+\mu^-$ differential production cross section	38
4.9.2	Non-prompt fraction	39
4.9.3	Reconstruction and trigger efficiency	39
4.9.4	Acceptance	40
4.10	Fitting procedure	41
4.11	Prompt J/ψ selection	44
4.12	Polarization template	45
4.13	Polarization fit	46
5	Results	48
5.1	Mass lifetime fit	49
5.2	Polarization fit	50
6	Conclusions	53

Chapter 1

Introduction

The J/ψ meson was discovered in 1974 by two research groups, one at Stanford Linear Accelerator Center led by Burton Richter [1], and one at Brookhaven National Laboratory headed by Samuel C.C. Ting [2]. Since then, several properties of this meson were measured such as branching ratios, cross sections of pp , $p\bar{p}$ at various energies. These measurements are important for understanding the production mechanisms of heavy quarks and their bound states, called quarkonia.

At present, there exist several production models, but all of them are not able to describe satisfactory all quarkonia properties. This thesis is devoted to the measurement of the quarkonia production in proton-proton collisions at $\sqrt{s} = 13$ TeV measured by the ATLAS detector. Special attention is given to the measurement of the polarization of directly produced J/ψ meson. The result of this measurement may refine the production models, which highly depend on the J/ψ polarization.

This analysis uses the 13 TeV data measured by the ATLAS detector. The ATLAS detector is a multipurpose detector which provides an excellent tool for B-physics measurements and analysis. The primary objective of this thesis is to lay ground for the basic steps needed for the measurement of J/ψ polarization. These steps will be the objective of further analysis. The first step is to show that the measured data are of sufficient quality and are suitable for polarization measurement. The data that meet these requirements are used for further measurements. A similar analysis was made by the CMS and LHCb collaboration at $\sqrt{s} = 8$ TeV, but the ATLAS data were not suitable for such analysis, because there were problems with angular distribution of decaying muons in B-physics triggers.

This analysis uses preliminary trigger efficiency maps and reconstruction maps produced by the BPHYS working group of ATLAS collaboration, but it is not an official J/ψ production cross section analysis.

Chapter 2

Theoretical background

2.1 Standard model

Particle physics is dealing with particles that are the constituents of what is usually referred to as matter and radiation. Many models were created to describe well known phenomena and physical laws. In the 1970s, the Standard Model (SM) of particles and their interactions was formed. This model is in the best agreement with experimental data. The Standard Model assumes, that our world is made of 17 elementary particles and their corresponding antiparticles. The first group is called fermions and it has a half-integer spin. The second group is named bosons and particles contained in it have integral spin. The particles interact via four known types of forces: electromagnetic, strong, weak and gravitational, of which the latter is not a part of the SM. The complete list of elementary particles and some of their properties is shown in table 2.1.

2.1.1 Fundamental interactions

Interactions in the Standard Model are realized as an exchange of mediating bosons, characteristic to the type of interaction between its constituents. Due to their character, they are frequently called exchange interactions.

Electromagnetic interaction is mediated by a massless photon and it has an infinite range. This interaction acts between charged particles. The theory describing the electromagnetic interaction is called quantum electrodynamics (QED) and it later laid the ground of the quantum field theory (QFT), the framework for description of other interactions in the Standard Model.

Strong interaction binds quarks together in hadrons and is mediated by the exchange of massless gluons. Strong force is the strongest force compared to other forces, and its range is limited to 1 fm.

	Symbol	Name	Mass	Charge	Spin
Quarks	u	up	$2.3^{+0.7}_{-0.5}$ MeV	2/3	1/2
	d	down	$4.8^{+0.5}_{-0.3}$ MeV	-1/3	1/2
	s	strange	95 ± 5 MeV	-1/3	1/2
	c	charm	1.275 ± 0.025 GeV	2/3	1/2
	b	bottom	4.18 ± 0.03 GeV	-1/3	1/2
	t	top	$173.07 \pm 0.52 \pm 0.72$ GeV	2/3	1/2
Leptons	e	electron	$0.510998928 \pm 0.000000011$ MeV	-1	1/2
	μ	muon	$105.6583715 \pm 0.0000035$ MeV	-1	1/2
	τ	tau	1776.82 ± 0.16 MeV	-1	1/2
	ν_e	e-neutrino	< 2 eV	0	1/2
	ν_μ	μ -neutrino	< 0.19 MeV	0	1/2
	ν_τ	τ -neutrino	< 18.2 MeV	0	1/2
Gauge bosons	γ	photon	0	0	1
	W^\pm	W	80.385 ± 0.015 GeV	± 1	1
	Z	Z	91.1876 ± 0.0021 GeV	0	1
	g	gluon	0	0	1
	H	Higgs	125.9 ± 0.4 GeV	0	0

Table 2.1: The list of particles in the Standard Model. The invariant mass, electric charge and spin is shown. [3,4]

Weak interaction is responsible for the relatively slow processes of β decay. The mediators of this interaction are W^\pm and Z^0 bosons. It is characterized by long lifetimes and small cross sections.

Gravitational interaction acts between all particles. Gravitational force is the weakest of all fundamental forces, and is almost 10^{-38} times weaker than strong interaction. Due to this fact, gravitational interaction is neglected in the SM. In some particle theories, this interaction is mediated by a hypothetical particle graviton with spin 2.

2.1.2 Quarks

Quarks are structureless fermions with spin 1/2 and are structural elements of mesons and baryons. Six quarks are known at present, as can be seen in table 2.1. Quarks exist in three generations. Almost all matter around us is made of u and d quarks, which belong to the first generation. In the 1960s, new particles were observed which decay slower than was expected. To these particles, an additional quantum number S called strangeness was assigned. After observation of c , b and t quarks, additional quantum numbers (charm, beauty and top) were assigned to baryons which carry these quarks. The first three quarks are referred to as light quarks q and the other three quarks are referred to as heavy quarks Q . All of the quarks, except top quark, bound to create

baryons and mesons. Because the mass of top quark is too large, it decays faster than it hadronizes and thus it can not be seen in any bound state.

2.1.3 Leptons

At present, six leptons are known, which are, similarly to quarks, categorized into three generations. There are three charged leptons and for each of them there is an electrically neutral neutrino. The masses or upper mass limits of leptons are given in table 2.1.

Neutrinos are specific with masses small in comparison to the corresponding charged leptons. Although the neutrinos have mass, in the Standard Model they are assumed to be massless. Another unique quality of neutrinos is that only negative projection of total angular momentum onto z axis was observed. This corresponds to a pure helicity¹ state $H = -1$ (left-handed). The latest measurement of the Planck detector provides the upper limit for the sum of neutrino masses m_{ν_i} [6]

$$\sum_i m_{\nu_i} < 0.25 \text{ eV.} \quad (2.1)$$

The proof of neutrino mass is a phenomenon called neutrino oscillation, where neutrinos with one flavor can convert to neutrinos with a different flavor. This process can not be done without the non-zero mass of the neutrino. Although the neutrino oscillation was predicted in 1957 by Bruno Pontecorvo [7], the first experimental evidence was made in 1998 at SuperKamiokande detector. [8]

2.1.4 Antiparticles

For every particle there exists a corresponding antiparticle with same mass and lifetime, but with the opposite charge and magnetic moment.

The existence of antiparticles is a general property of both fermions and bosons. The first observed antiparticle was the antiparticle of an electron, which is referred to positron. Due to the conservation laws, fermions must be created and destroyed in pairs. This mechanism is called pair-production and annihilation.

2.2 Strong interaction

2.2.1 Colour

The color is an additional internal degree of freedom of quarks. This degree of freedom was introduced after the observation of Δ^{++} baryon, which is made of three up quarks. This baryon would break the Pauli exclusion principle without introduction of another degree of freedom, called color charge. Thus, there are three colors red, green and blue with their respective anticolors. As stated above, strong interaction is mediated by an exchange of massless gluons. These gluons carry

¹Helicity is the projection of the spin \vec{S} onto the direction of momentum \vec{p} . [5]

color and anticolor charge and provide color interaction between two quarks. With three colors and three anticolors, there is a colored gluon octet $3 + 3 = 8 \oplus 1$, with possible combinations taking the form of

$$r\bar{b}, r\bar{g}, b\bar{g}, b\bar{r}, g\bar{r}, g\bar{b}, \frac{1}{\sqrt{2}}(r\bar{r} - b\bar{b}), \frac{1}{\sqrt{6}}(r\bar{r} + b\bar{b} - 2g\bar{g}), \quad (2.2)$$

and a colorless gluon singlet $\frac{1}{\sqrt{3}}(r\bar{r} + b\bar{b} + g\bar{g})$.

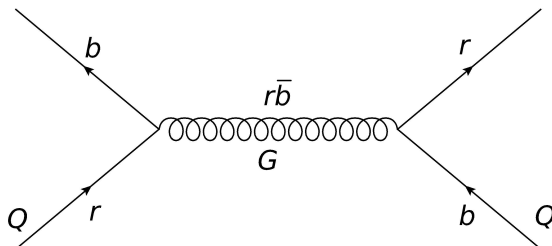


Figure 2.1: QQ' interaction via colored gluon exchange. The time runs from bottom to top.

The color charge of the strong interaction is analogous to the electric charge in the electromagnetic interaction. Both forces are mediated by massless vector particles, but compared to photons, gluons can interact with each other. This phenomenon is called gluon self coupling. Due to gluon self coupling, the color charge exhibits a particular behavior called antiscreening. It is the opposite to the screening of electric charge in QED as is illustrated in figure 2.2.

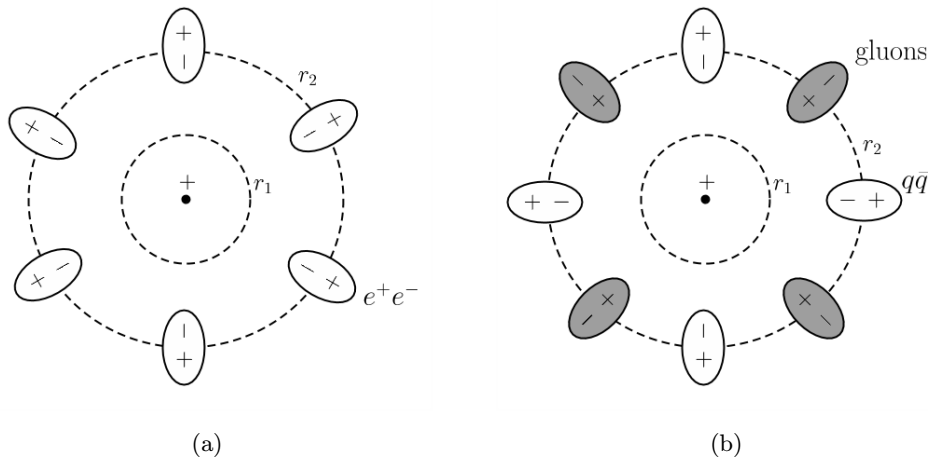


Figure 2.2: Screening of electric charge by virtual electron-positron pairs in (a) and antiscreening of the color charge by gluons and screening by quarks in (b). [9]

Both baryons and mesons must be colorless, thus quarks and gluons are confined inside hadrons. No free quarks were observed, with an exception of the top quark, which decays before it has a chance to hadronize.

2.2.2 QCD

The theory describing the interactions between quarks and gluons based on a color exchange is called quantum chromodynamics (QCD) and it is a part of Standard Model. The QCD is a non-Abelian theory represented by 3 matrices in the $SU(3)$ group. The non-Abelian behavior of the theory results in the self interaction of the gluons. The lagrangian of QCD can be written as

$$\mathcal{L}_{QCD} = \sum_f \bar{\psi}_i^{(f)} (i\gamma_\mu D_{ij}^\mu - m_f \delta_{ij}) \psi_j^{(f)} - \frac{1}{4} F_{\mu\nu}^a F_a^{\mu\nu}, \quad (2.3)$$

where the D_{ij}^μ is covariant derivative acting in color space, γ_μ are Dirac γ -matrices, ψ are quark field spinors, f correspond to the flavour of the quark and m corresponds to its mass. The covariant derivative for QCD has the following form

$$D_{ij}^\mu = \partial_\mu \delta_{ij} + ig_s t_{ij}^a A_a^\mu, \quad (2.4)$$

where A_a^μ represent gluon field, g_s is strong coupling and t_{ij}^a are the generators of the $SU(3)$ group. The field-strength tensor derived from A_a^μ looks like

$$F_{\mu\nu}^a = \partial_\mu A_\nu^a - \partial_\nu A_\mu^a - g_s f_{abc} A_\mu^b A_\nu^c, \quad (2.5)$$

where f_{abc} are the structure constants of the $SU(3)$.

Despite photons and gluons being massless, the QCD potential takes a different form due to the differences between those forces. The simplest potential model for mesons that describes strong interaction is called Cornell potential model, which takes the form of

$$V_s(r) = -\frac{4}{3} \frac{\alpha_s}{r} + kr, \quad (2.6)$$

where α_s is the strong interaction coupling and k is a free parameter. The first part of the equation is similar to the Coulomb potential with a factor of $\frac{4}{3}$. This factor arises from eight color gluon states averaged over three quark colors. The factor is divided by 2 from the definition of α_s . The second, linear term is associated with color confinement at large r , where k is the tension of color flux tubes.

The Cornell potential can be extended by inclusion of the spin interaction between quarks. These spin-dependent potentials are assumed to be dominated by a one-gluon exchange and consist of spin-spin, tensor and spin-orbit terms. For a system of two quarks, the potential takes the following form [10]:

$$V_{q\bar{q}} = -\frac{4}{3} \frac{\alpha_s}{r} + \sigma r + \frac{32\pi\alpha_s}{9m_q^2} \delta(r) \mathbf{S}_q \cdot \mathbf{S}_{\bar{q}} + \frac{1}{m_q^2} \left[\left(\frac{2\alpha_s}{r^3} - \frac{b}{2r} \right) \mathbf{L} \cdot \mathbf{S} + \frac{4\alpha_s}{r^3} \mathbf{T} \right], \quad (2.7)$$

where the \mathbf{L} is an orbital momentum, \mathbf{S}_q is a spin momentum of a particular quark, $\mathbf{S} = \mathbf{S}_q + \mathbf{S}_{\bar{q}}$

and \mathbf{T} is a tensor term.

These extended models give better results, but still they are not satisfactory. Thus, new interquark potential models are being developed and tested.

2.2.3 Running coupling

Charge screening in the QED (screening) and QCD (antiscreening) leads to the concept of a running coupling (the energy dependence of a strong coupling). In the QED, the coupling becomes large at (very) short distances and large energies, but its effect is small. In the QCD, the antiscreening effect causes the strong coupling to become small at a short distance (large momentum transfer). This causes the quarks inside hadrons to behave more or less like free particles. This property of the strong interaction is called asymptotic freedom.

On the other hand, at the increasing distance, the coupling becomes so strong that it is impossible to isolate a quark from a hadron. In addition, if the quark pair receives more energy than is necessary for the production of a new quark-antiquark pair, then it is energetically favourable to produce a new quark pair. This mechanism is called color confinement.

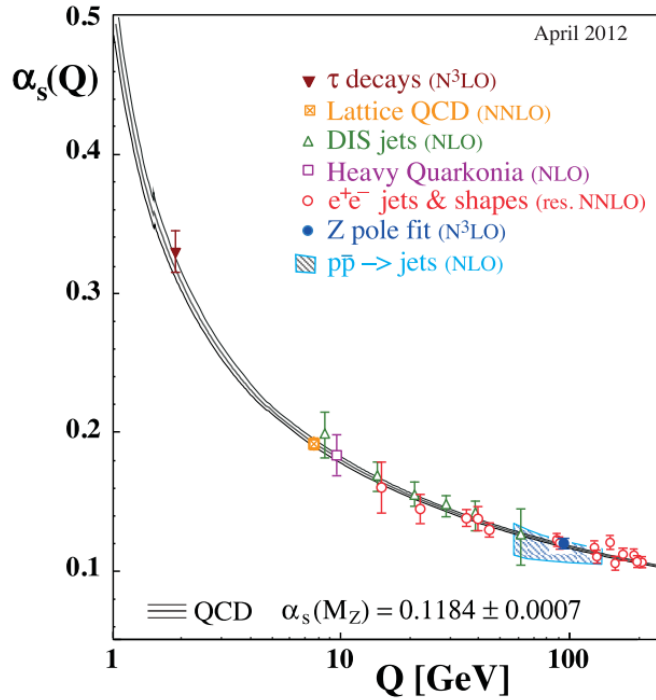


Figure 2.3: Summary of measurements of $\alpha_s(Q)$ as a function of the respective energy scale Q . The respective degree of the QCD perturbation theory used in the extraction of α_s is indicated in brackets (NLO: next-to-leading order; NNLO: next-to-next-to leading order; res. NNLO: NNLO matched with resummed next-to-leading logs; N³LO: next-to-NNLO)². [3]

Using perturbative QCD (pQCD) calculations and experimental data, the coupling constant of

the QCD can be shown to have the following energy scale-dependence

$$\alpha_s(Q) = \frac{2\pi}{\beta_0 \ln \frac{Q}{\Lambda_{\text{QCD}}}}, \quad (2.8)$$

where $\beta_0 = 11 - \frac{2}{3}n_f$, with n_f being the number of the active quark flavor, and Λ_{QCD} is the QCD scale [3]. The value of $\Lambda_{\text{QCD}} = (0.339 \pm 0.010)$ GeV is determined by experiments. This dependence is valid only for $Q^2 \gg 2\Lambda^2$, where Q is the transferred momentum. The summary of measurements of $\alpha_s(Q)$ from multiple experiments is shown in Figure 2.3.

2.3 J/ψ meson

The existence of the c quark was predicted by S. Glashow, J. Liopoulos and L. Maiani in 1970. Two separate groups led by Samuel C.C. Ting [2] and Burton Richter [1] participated in the discovery of J/ψ and therefore a c quark. They observed a vector meson with higher mass than then known ω , ρ and φ vector mesons consisting of lighter quarks. The first group named the new meson J while the second ψ . Both groups announced their discoveries on 11th November 1974. Thus, the new particle was named J/ψ .

Since the observation of J/ψ meson, many of its properties were precisely measured. The most important parameters are mass of (3096.916 ± 0.011) GeV and width (92.9 ± 2.9) keV. In hadron collisions, the J/ψ is primarily produced by the gluon fusion as can be seen in Figure 2.4, but it can also be found in the decay chain of heavier particles such as B mesons. Most probably, the J/ψ decays into hadrons, but for measurement the lepton channel is used more often. The decay modes with its branching ratio are presented in table 2.2

Decay modes	
hadrons	$(87.7 \pm 0.5)\%$
virtual $\gamma \rightarrow$ hadrons	$(13.50 \pm 0.30)\%$
ggg	$(64.1 \pm 1.0)\%$
γgg	$(8.8 \pm 0.5)\%$
e^+e^-	$(5.94 \pm 0.06)\%$
$\mu^+\mu^-$	$(5.93 \pm 0.06)\%$

Table 2.2: The most probable decay modes of the J/ψ meson with its branching ratios. [3]

2.3.1 J/ψ polarization

The polarization of massive vector particle measures the degree to which the spin of a given particle is aligned with respect to a chosen axis. The polarization can be measured through the

²NLO etc. are the levels of the perturbation QCD theory into which the Feynman diagrams are counted.

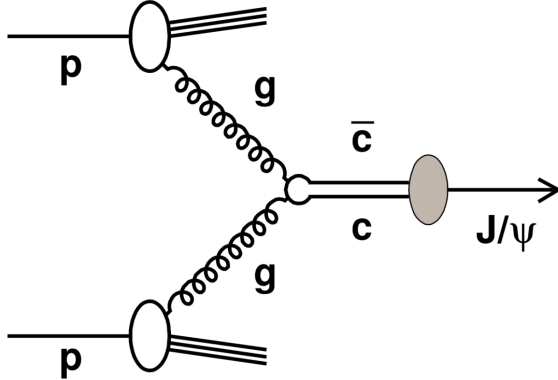


Figure 2.4: An example of hadro-production of the J/ψ meson. The J/ψ is produced in the subprocess $g + g \rightarrow J/\psi$ in pp collision. [11]

study of the angular distribution of the leptons produced in their $\mu^+\mu^-$ decay. In this channel the differential cross-section as function of the muons angular variables in the rest frame of the J/ψ can be described as follows [12]

$$\omega_i = \frac{1}{1 + \frac{\lambda_\theta}{3}} (1 + \lambda_\theta \cos^2 \theta^* + \lambda_\phi \sin^2 \theta^* \cos 2\phi^* + \lambda_{\theta\phi} \sin 2\theta^* \cos \phi^*), \quad (2.9)$$

where θ^* is the angle between the direction of the positive muon momentum in the J/ψ decay and z axis of the chosen polarization frame. ϕ^* is an azimuthal angle and depends on the coordinate system which is described in figure 2.5. λ_θ , λ_ϕ and $\lambda_{\theta\phi}$ are related to the spin density matrix elements of the dimuon spin wave function. There exist frame invariant polarization parameter $\tilde{\lambda}$ [13], which is defined as

$$\tilde{\lambda} = \frac{\lambda_\theta + 3\lambda_\phi}{1 - \lambda_\phi}. \quad (2.10)$$

There are several choices of polarization frames (figure 2.6) characterized by different quantization axis in the production plane. The first one, centre-of-mass helicity (HX) frame, where the z axis coincides with the direction of the J/ψ is the most commonly used. The Collins-Soper frame [14] defines the axis as the bisector of the angle between two beam directions in the J/ψ rest frame and the perpendicular helicity (PX) frame [15], with the z axis orthogonal to that in the CS frame. The Gottfried-Jackson frame (GJ) [16] defines the polar axis in the direction of the momentum of one of the two colliding beams.

In the past, there were several measurements of J/ψ polarization especially in the low p_T region. The CMS collaboration measured the J/ψ polarization at LHC at $\sqrt{s} = 7$ TeV conditions in similar fiducial region as the ATLAS. The CMS results are shown in figure 2.7.

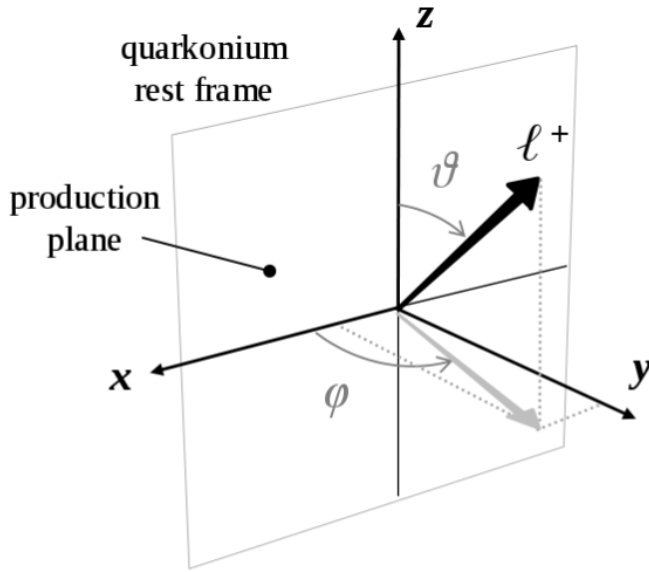


Figure 2.5: The coordinate system for the measurement of a two-body decay angular distribution in the quarkonium rest frame. The y axis is perpendicular to the plane containing the momenta of the colliding beams. The polarization axis z is chosen according to one of the possible conventions described in figure 2.6. [12]

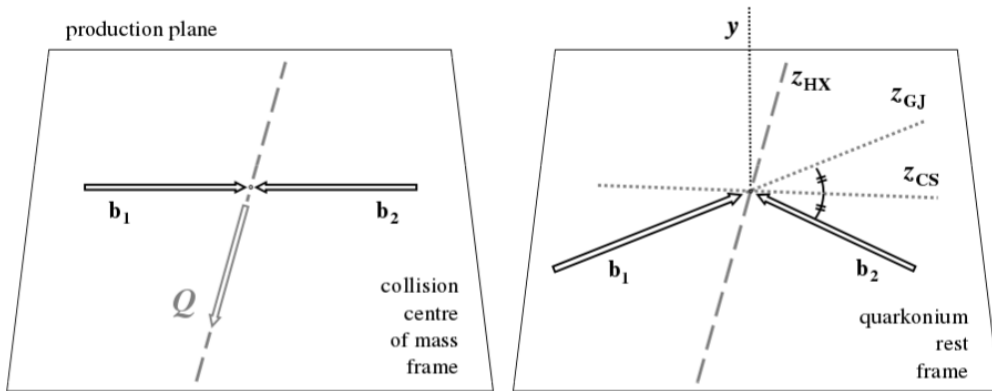


Figure 2.6: Illustration of the three definitions of the polarization axis z with respect to the directions of motion of the colliding beams (b_1 , b_2) and the quarkonium (Q), where CS stands for Collins-Soper, GJ for Gottfried-Jackson and HX is for helicity frame. [12]

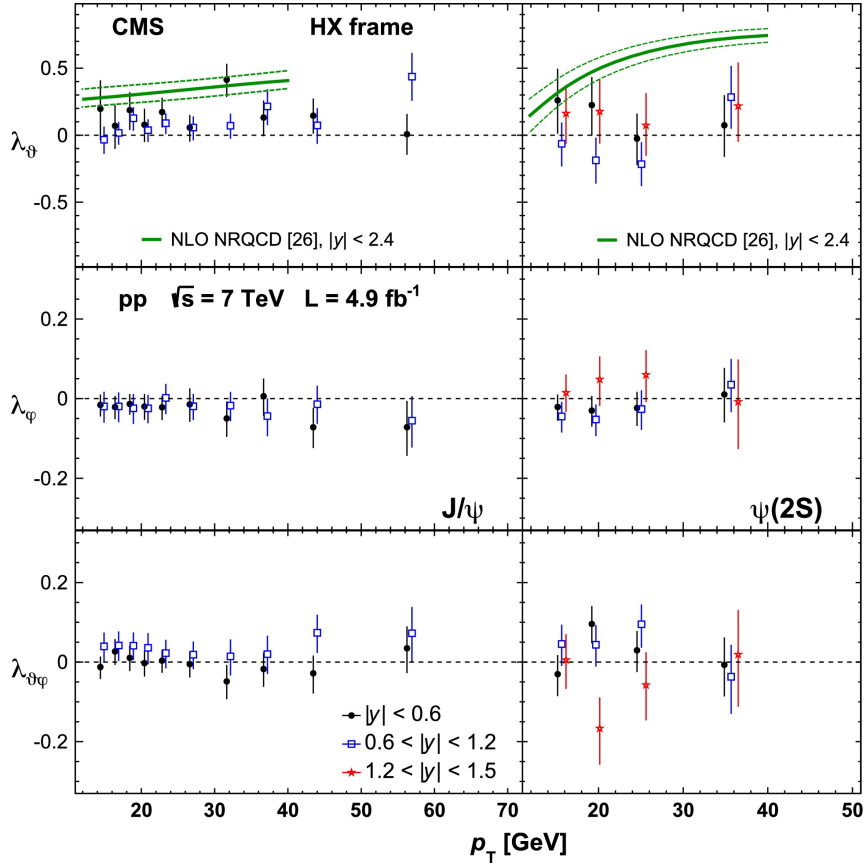


Figure 2.7: CMS measurement of polarization parameters versus p_T for J/ψ (left) and $\psi(2S)$ (right) in different bins of rapidity and frames of reference. The results are in agreement with zero polarization scenario. [17]

2.4 Heavy quarkonia production

The quarkonia are bound states of $Q\bar{Q}$ pair made of quarks of the same flavour. The combined pair is flavourless and its energy-level structure is reminiscent of positronium. A designation heavy quarkonia is usually attributed to Charmonium ($c\bar{c}$) and Bottomonium ($b\bar{b}$). The top quark does not occur in hadrons due to its large mass and short lifetime, it decays before it has the chance to hadronize.

The charmonium spectrum contains several resonances as can be seen in figure 2.8. In the system, there exist kinematic threshold called $D\bar{D}$. The states under $D\bar{D}$ threshold decay via di-lepton channel with high probability and it is easy to detect them, but if binding energy exceeds the energy of $u\bar{u}$ quark pair, then it will decay with high probability by strong interaction into D and \bar{D} mesons. The main parameters and quantum numbers of resonances under $D\bar{D}$ threshold are listed in table 2.3.

Since quarkonia are almost nonrelativistic, they also have spectrum similar to the hydrogen

predictions which struggle to describe strong interaction in the low energy region close to the non-perturbative boundary.

Most theories, such as factorization theorem, agree that the non-perturbative and perturbative part of the heavy quarkonium model can be separated. It also agree that the production rates can be factorized into the product of a short-distance factor describing the production of the heavy quark pair and a long-distance factor describing the formation of the bound state. The models mainly differ by the factorization method. Three most prominent models [18], the Color Evaporation Model, the Color Singlet Model and the Nonrelativistic QCD Factorization Model, suggest very different factorization techniques.

The factorization theorem [19] for the Drell-Yan process $A + B \rightarrow \mu^+ + \mu^- + X$ is defined as

$$\sigma_{AB} = \sum \int d\xi_A d\xi_B f_a^A(\xi_A, \mu) \sigma_{ab}^{AB} \left(\frac{x_A}{\xi_A}, \frac{x_B}{\xi_B}, Q; \frac{\mu}{Q}, \alpha_s(\mu) \right) f_b^B(\xi_B, \mu), \quad (2.11)$$

where the σ_{ab}^{AB} is the ultraviolet-dominated hard scattering cross section of two partons a , b , computable in perturbation theory. The f_x^X is parton distribution function and μ_X renormalization scales used in the calculation of σ_{ab}^{AB} .

2.4.1 Color Singlet Model

In the Color Singlet Model (CSM) [20], the perturbative and non-perturbative parts of the quarkonium production process are completely correlated. In this model, the $Q\bar{Q}$ pair is directly prepared with the proper quantum numbers in the initial hard subprocess, only then is non-zero probability to form the corresponding final state. The gluons can not adjust quantum numbers in this theory and they only serve to generate the binding potential. The schematic diagram of J/ψ produced in the CSM is illustrated in figure 2.9.

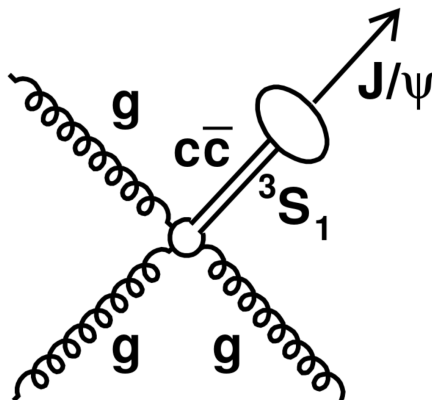


Figure 2.9: The schematic diagram for J/ψ production in the Color singlet Model. [11]

The CSM correctly predicts the normalization and momentum dependence of the J/ψ photoproduction rate, but it fails to adequately reproduce other available data on quarkonium production. Its predictions of the directly produced J/ψ and $\psi(2S)$ hadro-production rates are smaller by more than an order of magnitude.

2.4.2 Color Evaporation Model

In the Color Evaporation Model (CEM) [18,21], the perturbative and non-perturbative parts of the quarkonium production process are considered to be uncorrelated. The production cross section of all quarkonia states in CEM is some fraction of the overall $Q\bar{Q}$ pairs cross section below the $H\bar{H}$ threshold, where H is the lowest mass hadron with corresponding heavy quark. The CEM cross section is then simply the $Q\bar{Q}$ production cross section with a cut on the pair mass. In the CEM there are not any constrains on the color or spin of the final state, because the produced $Q\bar{Q}$ pair neutralizes its color by interaction with the collision-induced color field, thus the name "color evaporation". The interaction with color field can be described by the multiple soft gluon emissions. The soft interactions are assumed to be universal and the effect on the dynamics of the quarkonium state is negligible. The schematic diagram of J/ψ produced in the CEM is illustrated in figure 2.10.

The CEM predicts zero polarization of the J/ψ which is valid only for the low p_T regions.

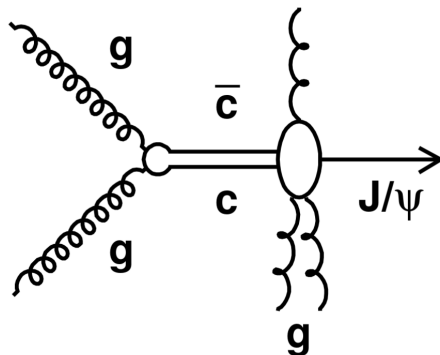


Figure 2.10: The schematic diagram for J/ψ production in the color evaporation model. [11]

2.4.3 Nonrelativistic QCD Factorization Model

The Nonrelativistic QCD Factorization Model is based on the effective field theory Nonrelativistic QCD (NRQCD) [18] and lies somewhere between the previous two models. It predicts non-zero probability for any quark pair to produce almost any quarkonium state, but the probability depends

on the initial quantum state. The schematic diagram of J/ψ produced in the NRQCD is illustrated in figure 2.11.

The quarkonium production cross section, in the NRQCD factorization model, can be written as

$$\sigma(H) = \sum_n \frac{F_n(\Lambda)}{m_Q^{d_n-4}} \langle 0 | \mathcal{O}_n^H | 0 \rangle, \quad (2.12)$$

where H is the quarkonium state Λ is the ultraviolet cutoff of the effective theory, the F_n are short-distance coefficients, and the \mathcal{O}_n^H are four-fermion operators, whose mass dimensions are d_n .

The short-distance coefficients $F_n(\Lambda)$ are essentially the process-dependent partonic cross sections to make a $Q\bar{Q}$ pair. The $Q\bar{Q}$ pair can be produced in a color-singlet state or in a color-octet state. The short-distance coefficients are determined by matching the square of the production amplitude in the NRQCD to the full QCD. Because the $Q\bar{Q}$ production scale is of the order of m_Q or greater, this matching can be carried out in perturbation theory.

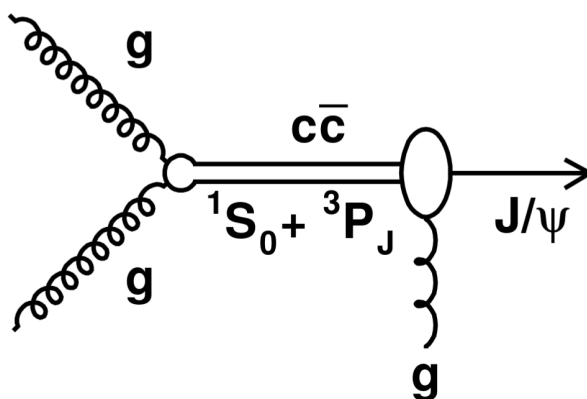


Figure 2.11: The schematic diagram for J/ψ production in the color octet model. [11]

The Nonrelativistic QCD Factorization Model successfully reproduced various quarkonia data and fits well on the experiment, but there are still some problem areas. In the figure 2.12, the NRQCD prediction of prompt J/ψ cross section is compared to CSM prediction and the LHCb data. Recently, the proof of the factorization in heavy quarkonium production in NRQCD Factorization Model was introduced at next-to-next-to-leading order (NNLO) in coupling constant by using diagrammatic method of QCD [22].

2.4.4 k_t -factorization approach

This factorization method is based on another description of the structure function, when incident gluons have non-zero transverse momenta in small- x region. This non-zero transverse momentum

is the result of the diffusion of parton evolution.

The exact expression for k_t gluon distribution can be obtained as a solution of the evolution equation which, contrary to the parton model case, is nonlinear due to interactions between the partons in small- x region.

The biggest advantage compared to the classical parton model is that the main part of the NLO and even NNLO corrections is effectively included in the k_t -factorization approach, due to the off-shell gluons. [23]

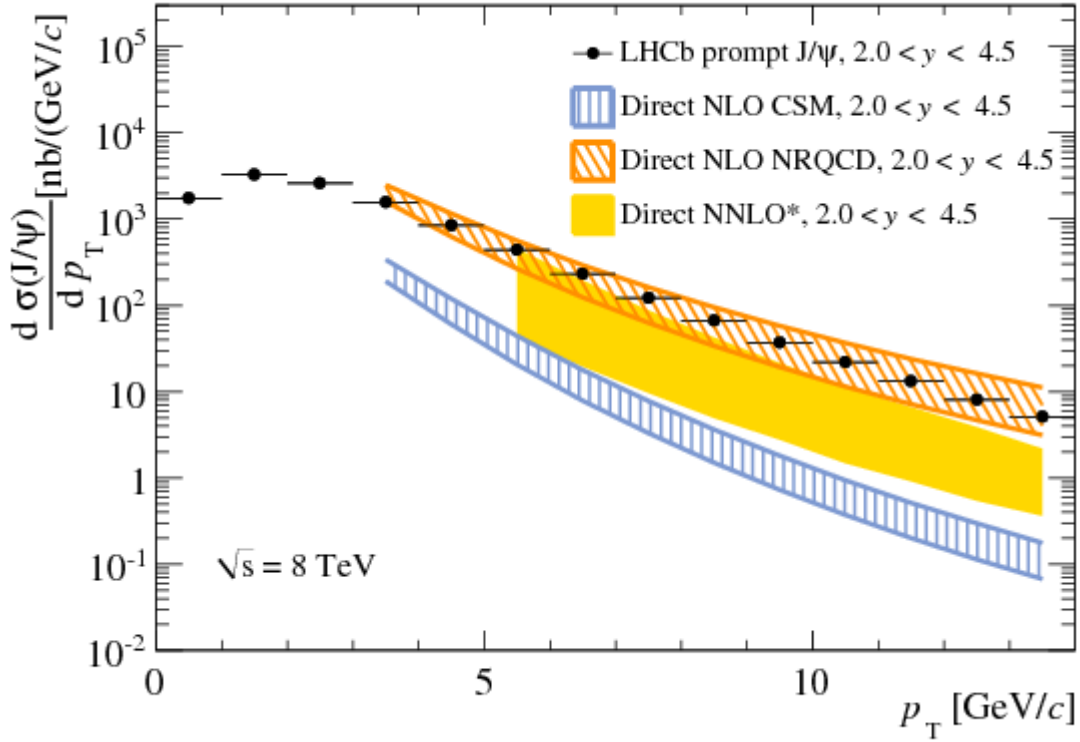


Figure 2.12: The model predictions of differential production cross section compared with data measured at LHCb experiment. [24]

2.5 B-physics

The B physics is a common name for physics focusing on the measurement of processes which contain at least one beauty quark. Since the discovery of beauty quark in 1977 by the Fermilab E288 experiment team led by Leon M. Lederman, the B-physics was an area of many discoveries. In the early days after the discovery, the primary objective was to determine the basic features of the bottom quark, such as lifetime, branching fractions, $B^0 - \bar{B}^0$ mixing or V_{ub}/V_{cb} ratio. After that, the main objective changed to use the bottom quark to probe the Standard Model, and search for physics Beyond the Standard Model. [25]

At the ATLAS experiment, the B-physics working group brings together b and c physics heavy quarkonia, and the physics of any low mass states. The physics program includes the new physics search, such as measurement of the CP-violating phase θ_s of the B_s^0 system, searching for anomalous rates of the rare B-decay channel $B_s^0 \rightarrow \mu^+ \mu^-$, as well as precise tests of QCD by studying the production mechanisms of $b\bar{b}$ pairs, beauty baryon polarization, and lifetime measurement. The strategy of ATLAS for B-physics strongly depends on the ATLAS trigger system decision which will be different in various luminosity periods. [26]

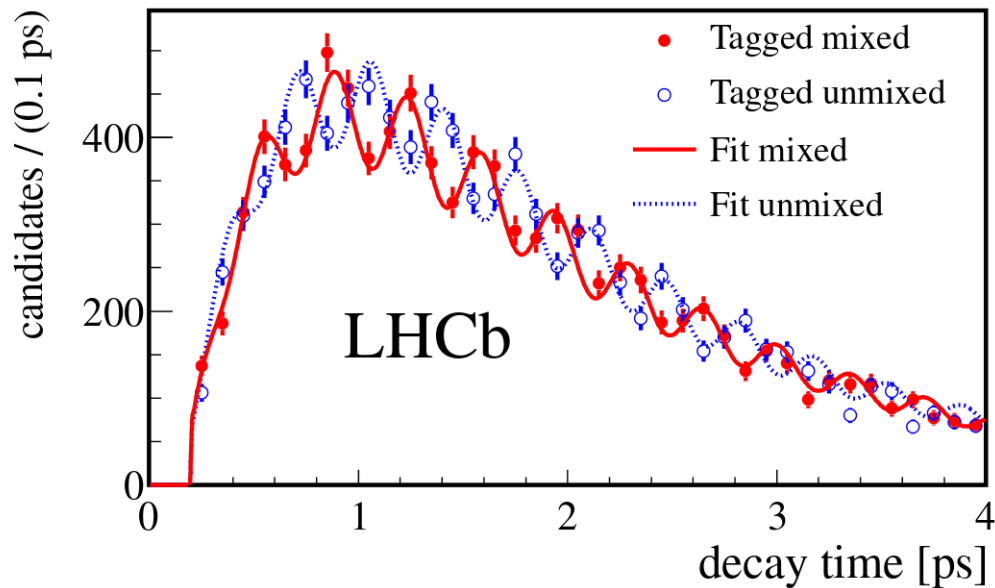


Figure 2.13: Decay time distribution fit for mixed and unmixed events in the $B_s^0 \rightarrow D_s^- \pi^+$. [27]

Chapter 3

The LHC and ATLAS detector

At present, the LHC (Large Hadron Collider) is the largest particle accelerator in the world. It is located in the CERN laboratory near Geneva, Switzerland. The LHC is designed to provide proton-proton collisions with $\sqrt{s} = 14 \text{ TeV}$ with a design luminosity of $10^{34} \text{ cm}^{-2} \text{ s}^{-1}$ and bunch collision rate of 40 MHz.

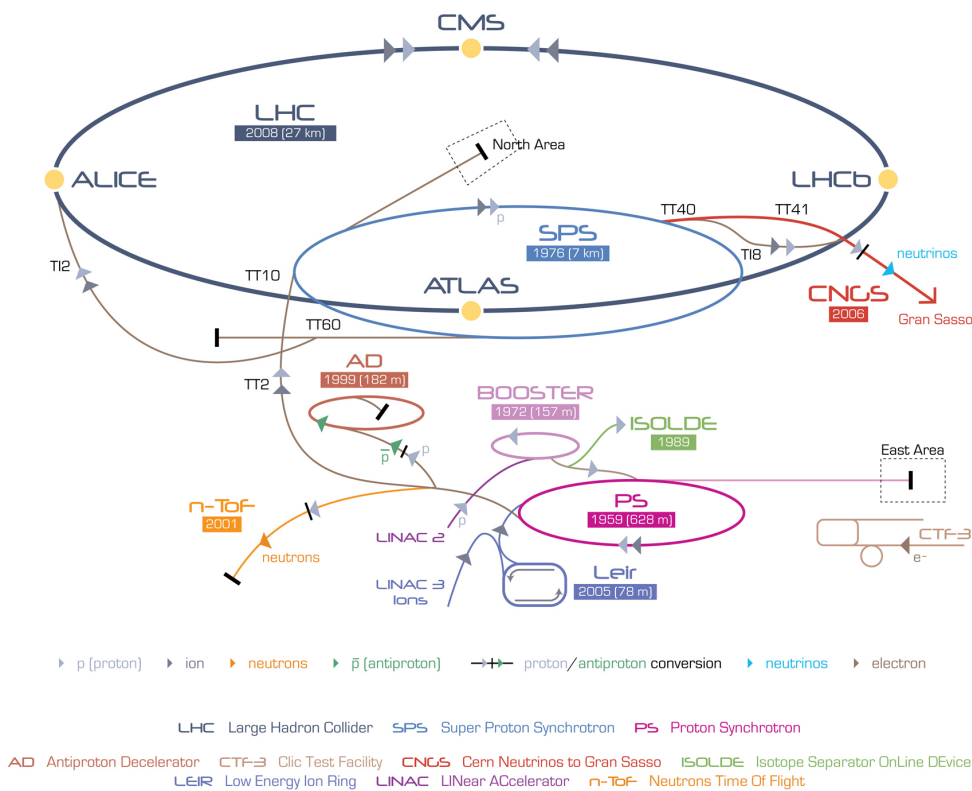


Figure 3.1: The LHC Complex. The injection chain including all pre-accelerators. [28, 29]

However, during the first run period, the LHC was operating at lower energy of $\sqrt{s} = 7$ TeV in 2011 and $\sqrt{s} = 8$ TeV in 2012. The achieved collision rate of 20 MHz, which corresponds to 50 ns bunch spacing was also lower than designed one.

Parameter	unit	2010	2011	2012	2015
E_B	TeV	3.5	3.5	4	6.5
Spacing	ns	150	50	50	25
N_p	$\times 10^{11}$	1.2	1.45	1.7	1.2
N_B	-	368	1380	1380	2780
\mathcal{L}	$\times 10^{33} \text{ cm}^{-2} \text{ s}^{-1}$	0.21	3.7	7.7	8.6
$\langle \mu \rangle$	-	4	17	37	23
β^*	m	3.5/ 2	1.5/ 1	0.6	0.8

Table 3.1: Summary of the main LHC beam and machine parameters for 2015 at IR1, where the $\langle \mu \rangle$ is mean number of multiple pp interactions per bunch crossing and β^* denotes the optical β function, N_B is total number of bunches, E_B is beam energy, N_p is number of protons per bunch and \mathcal{L} is peak luminosity. [30] [31]

During the first long shutdown in 2013 and 2014, the apparatus has undergone considerable improvements which enables higher energies and collision rate of 40 MHz. Because of slow progress with training of superconducting magnets it was decided that the LHC will run in 2015 at $\sqrt{s} = 13$ TeV, almost design energy.

The LHC complex houses four major experiments ALICE, ATLAS, CMS, LHCb and several smaller ones. The concrete list of experiments at LHC complex can be found in [32].

3.1 ATLAS detector

The ATLAS (A Toroidal LHC ApparatuS) detector is general-purpose detector designed to study pp collisions at the LHC. The main area of research is Standard Model measurement, dedicated top quark studies, precise study of electroweak theories, SUSY (supersymmetry), and searches for any new physics. In 2012, ATLAS and CMS collaborations announced the discovery of the Higgs boson with a mass of (125.9 ± 0.4) GeV. The ATLAS subdetectors covers almost full solid angle around the collision point and are symmetric in the forward-backward direction with respect to the interaction point. The subdetectors can be geometrically divided into barrel section, two end-caps and two forward regions. In the forward region there can be found ALFA, LUCID and ZDC sub-detectors which primary serve for luminosity measurement. The non-forward subdetectors can be divided into three sections inner detector (ID), calorimetry systems and muon spectrometer (MS). The detectors are immersed in the magnetic field that bends charged particle trajectories and allows momentum measurement [33].

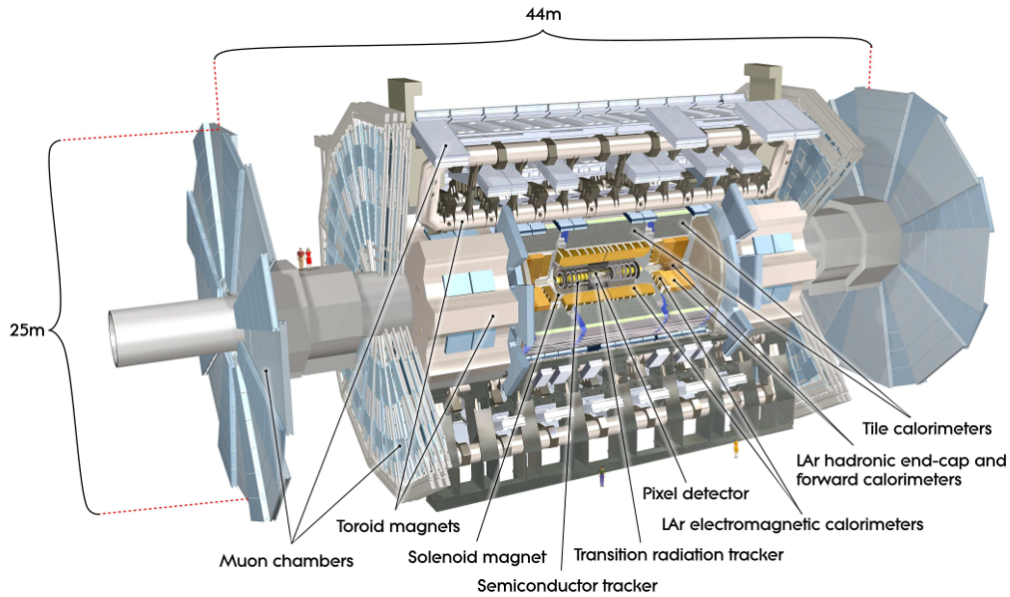


Figure 3.2: ATLAS detector cut-away view with its subdetectors highlighted. [33]

3.2 Coordinate system

The coordinate system describing the detector phase space is usually set up with the z -axis parallel to the beam direction and the x - y plane transverse to the beam direction. The variables measured in the transverse plane are denoted with a T subscript. The positive x -axis is defined as pointing from the interaction point to the center of the LHC ring, the positive y -axis is defined as pointing upwards. The positive direction of z -axis is defined so as to create the right-handed coordinate system.

For the track measurement, it is easier to determine the azimuthal angle Φ , which is measured around the beam axis, and the polar angle Θ , which is an angle between the beam axis and the measured point. Using this phase space description, the following terms are introduced.

The pseudorapidity is defined as

$$\eta = -\ln \tan \frac{\Theta}{2}. \quad (3.1)$$

In the case of massless nonrelativistic objects, the pseudorapidity is equal to the rapidity

$$y = \frac{1}{2} \ln \frac{E + p_z}{E - p_z}. \quad (3.2)$$

The distance ΔR in the pseudorapidity-azimuthal angle space is defined as

$$\Delta R = \sqrt{\Delta\eta^2 + \Delta\Phi^2}. \quad (3.3)$$

3.3 Magnet system

The ATLAS magnet system is unique with respect to other experiments at LHC and is necessary to the momentum measurement of charged particles. The ATLAS magnet system is composed of four parts: central solenoid, barrel toroid and two end-cap toroids [34].

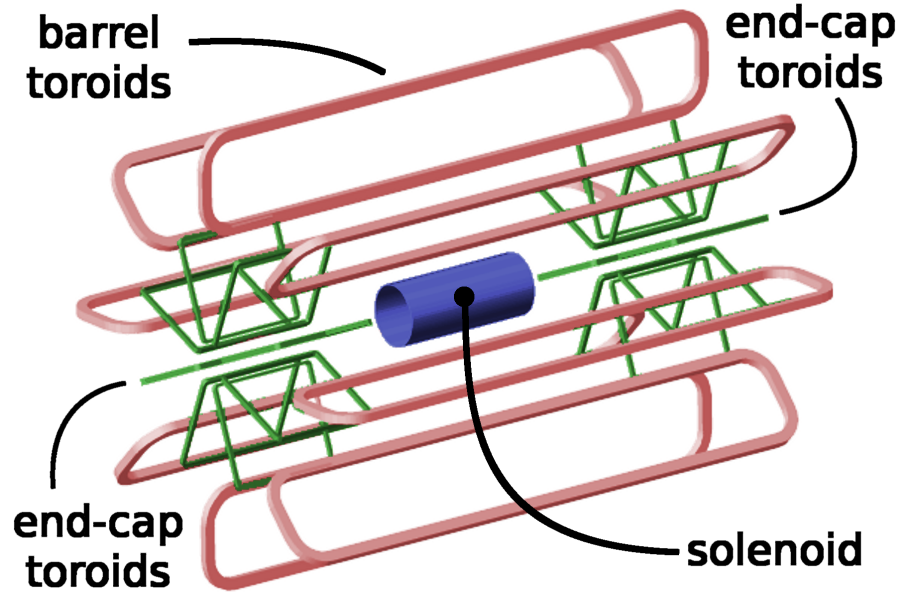


Figure 3.3: ATLAS magnet systems [35]

The central solenoid [36] is designed to provide 2 T magnetic field in central tracking region. To achieve that, the superconducting solenoid with radius 1.247 m and length of 5.283 m is used. In the nominal state, the coil is supplied with 7730 A and whole solenoid is cooled up to 4.5 K using liquid helium as a coolant.

The barrel toroid consists of 8 flat superconducting race-track coils, each 25.3 m long and 5 m wide, grouped in a torus shape with inner bore of 9.4 m and outer diameter of 20.1 m. The nominal magnetic field inside torus is 4 T and similarly to central solenoid the supply current is 21 kA and operation temperature is 4.7 K.

The end-caps toroids, positioned inside the barrel toroid at both ends of the central solenoid, provide the required high magnetic field across a radial span of 1.5 to 5 m.

3.4 Inner detector

The inner detector is designed to provide an excellent momentum resolution for charged particles and both primary and secondary vertex position measurements with high precision in the pseudo-rapidity range of $|\eta| < 2.5$. The ID has to withstand high-radiation environment as the innermost subsystem of the ATLAS detector.

The ID is contained within a cylindrical envelope of a length of ± 3512 mm and of a radius of 1150 mm, and is immersed in a 2 T magnetic field generated by the central superconducting solenoid. The ID consists of a silicon pixel detector, a silicon strip detector (SCT) and a transition radiation tracker (TRT).

As can be seen in figure 3.4, the detectors are arranged as concentric cylinders around the beam axis in the barrel region. In the end-cap regions, there are pixel modules located on disks perpendicular to the beam axis. All detectors are mounted on a support structure, which is made of carbon fibers to ensure good mechanical properties, thermal conduction and low material budget.

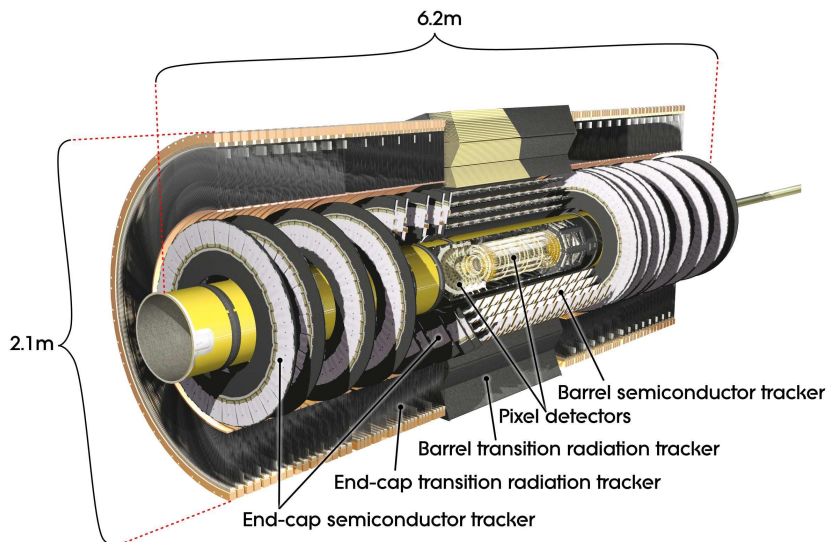


Figure 3.4: The schematic cut-away view of ATLAS inner detector. [33]

3.4.1 Pixel Detector

The Pixel detector contains three layers of the pixel modules in the barrel region (called ID layers 0–2) and two end-caps, each with three disk layers. The 0th layer is also referred to as B-layer. The layers are equipped by silicon pixel detectors with nominal pixel size of $50 \times 400 \mu\text{m}^2$. The sensor thickness is approximately $250 \mu\text{m}$. Silicon pixel sensors use planar technology with oxygenated n-type wafers and are read out on the n^+ -implanted side of the sensor. The opposite side of the electrodes is in contact with a p^+ layer. Each pixel sensor is bump-bonded through hole in the

sensor passivation layer to front-end readout chip FE-I3. The pixel detector provides approximately 80.4 million readout channels in total.

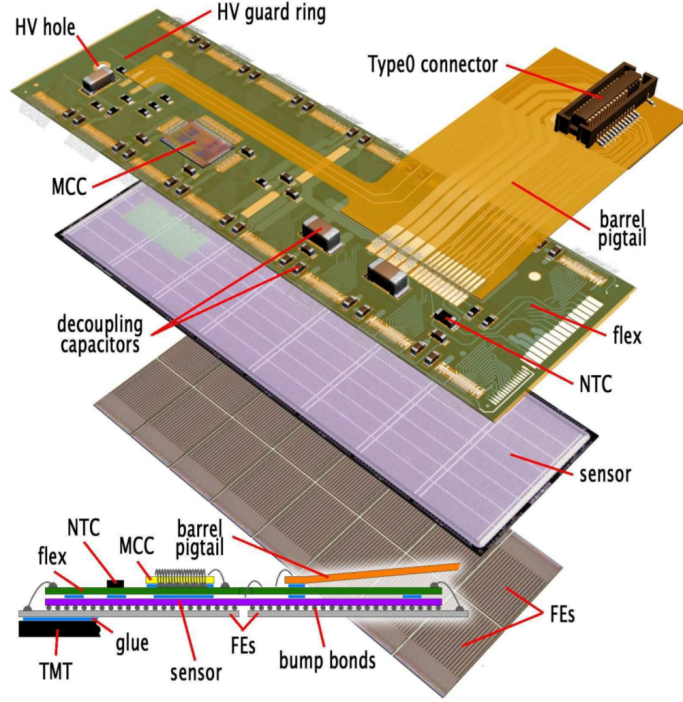


Figure 3.5: Schematic view of a barrel pixel module illustrating the major pixel hybrid and sensor elements, including the MCC (module-control chip), the front-end (FE) chips, the NTC thermistors, the high-voltage (HV) elements and the Type0 signal connector. [33]

During the first long shutdown (LS0) between years 2013 and 2015, upgrades were made and the fourth layer of the pixel detector was added. This layer is placed between new smaller beryllium beampipe with radius of 25 mm and current B-layer. It is called Insertable B-layer (IBL). This IBL is equipped with new sensors using planar n^+ -in- n and 3D double-sided n^+ -in- p technology and in total it adds 12 million channels to the existing Pixel Detector. These sensors have finer granularity of $50 \times 250 \mu\text{m}^2$ and besides higher radiation tolerance, new readout chip FE-I4 has lower noise and power consumption. The IBL will further improve tracking robustness, vertexing and b tagging performance. During first period of data taking in 2015 at $\sqrt{s} = 13 \text{ TeV}$ the data measured by the IBL are in agreement with simulations and thus IBL proved its good performance [37]. The improvement of primary vertexing is the most significant in the transverse impact parameter $\sigma(d_0)$ (figure 3.6) which improved to almost twice compared to 8 TeV measured without IBL.

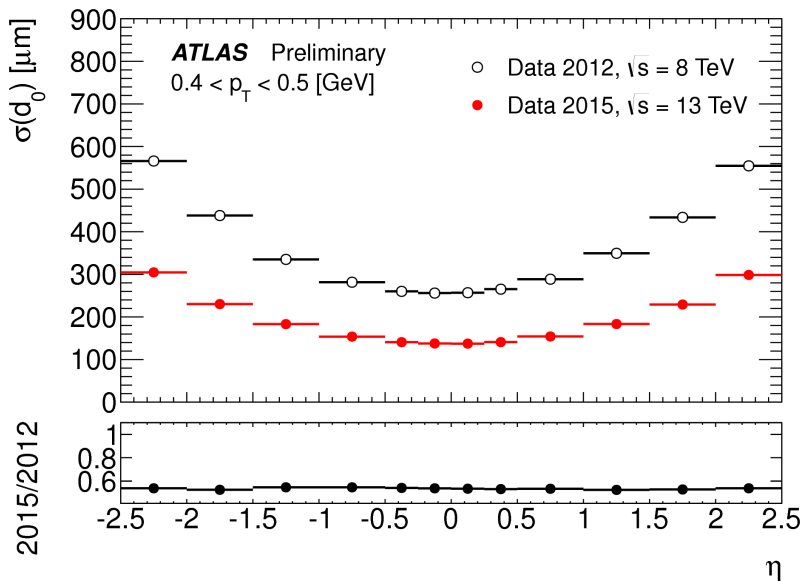


Figure 3.6: Unfolded transverse impact parameter resolution measured in 2015 at $\sqrt{s} = 13$ TeV, with the Inner Detector including the IBL. The plots are shown as a function of η , for values of $0.4 < p_T < 0.5$ GeV compared to that measured from data in 2012, $\sqrt{s} = 8$ TeV.

3.4.2 SCT detector

SCT detector consist of four layers of double detectors in the barrel region (called ID layers 3–6) and two end-cap regions, each containing nine layers. Layers are equipped by modules which consist of $80 \mu\text{m}$ pitch micro-strip sensors with thickness $285 \pm 15 \mu\text{m}$, providing $R - \Phi$ coordinates.

Every two sensor modules are glued together in the barrel region within a hybrid module. On one detector layer, there are 2 sensor layers rotated within their hybrids by ± 20 mrad around the geometrical center of the sensor to measure both $R - \Phi \times z$ coordinates.

For reason of cost and reliability, the sensors of SCT use classic single-sided p⁺-in-n technology. The sensors are connected to a binary signal readout chips. In total, the SCT provides approximately 6.3 million readout channels.

3.4.3 Transition radiation tracker

Main purpose of TRT is to measure transition radiation of charged particles, in order to distinguish between light electrons and other particles, in the pseudorapidity range of $|\eta| < 2.0$. The TRT consist of 73 layers of straws in the barrel region and 160 straw planes in end-cap. Typically, the TRT gives 36 hits per track, but it provides only $R - \Phi$ information.

The basic TRT detector elements are polyamide drift straw tubes with diameter of 4 mm filled by special gaseous mixture. The straw tube walls operates as cathodes, while the $31 \mu\text{m}$ thick tungsten wire plated with $0.5 \mu\text{m}$ – $0.7 \mu\text{m}$ layer of gold operates as anode. The total number of readout channels of TRT is approximately 351,000.

3.5 Calorimetry

Calorimetry system is designed to provide good energy resolution for measurement of electromagnetic and hadronic showers, and it must also limit punch-through into the muon system. Calorimetry system consist of two separate calorimeters using different designs suited to the widely varying requirements of the physics processes of interest, and it cover region up to $|\eta| < 4.9$. Over the η region matched to the inner detector, the fine granularity of the EM calorimeter is ideally suited for measurements of electrons and photons. There is coarser granularity in the rest of the detector, but calorimeters are precise enough to satisfy the physics requirements for jet reconstruction and E_T^{miss} measurement.

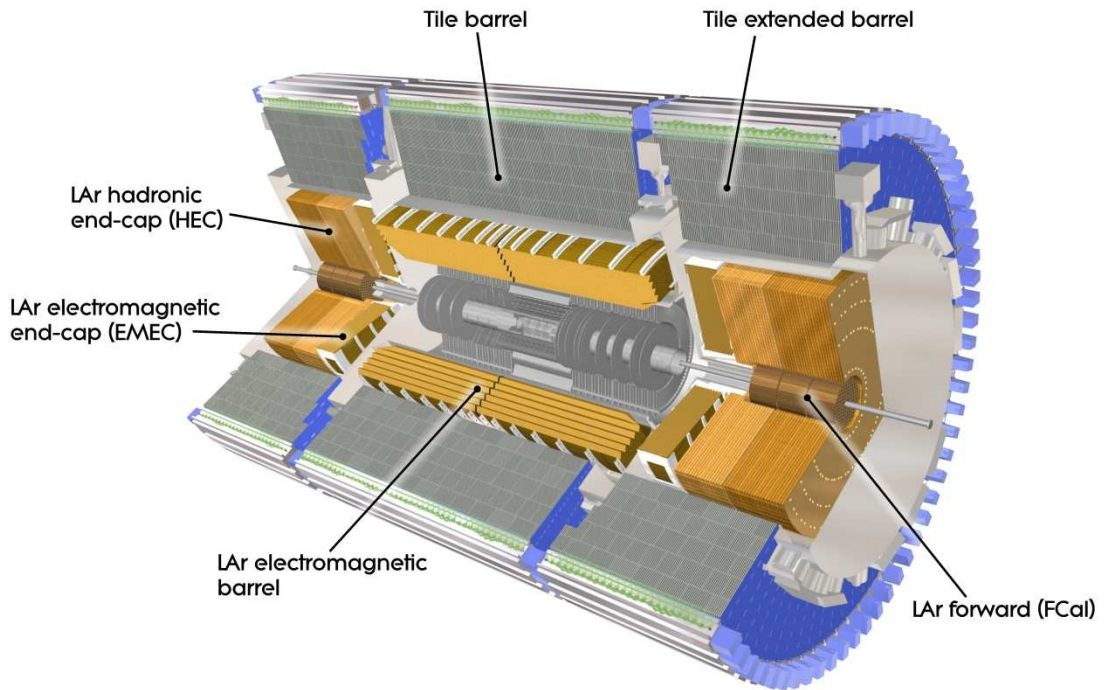


Figure 3.7: ATLAS calorimetry system cut-away view. [33]

Electromagnetic calorimeter (ECAL) at ATLAS is lead-liquid argon (LAr) detector with accordion-shaped kapton electrodes and lead absorber plates. The readout electrodes are located in the gaps between the absorbers and consist of three conductive copper layers separated by insulating polyamide sheets. The overall thickness of the ECAL is between 24 and 26 radiation lengths.

Hadronic calorimeter is placed directly outside the EM calorimeter envelope. The two different calorimeter types are used to detect hadronic showers. Scintillator tile calorimeter(TileCal) is a sampling calorimeter using steel as the absorber and plastic scintillating tiles as the active material and LAr Hadronic End-cap Calorimeter (HEC) uses similar design as ECAL, but as a absorber uses copper instead of lead.

3.6 Muon spectrometer

The muon system is designed to detect charged particles exiting the barrel and end-cap calorimeters, and to measure muon momentum in the pseudorapidity range of $|\eta| < 2.7$. It measures properties of muon tracks bent by the large superconducting air-core toroid magnets. Detectors are situated in the barrel, end-cap and also in the transition regions ($1.4 < |\eta| < 1.6$), where the tracks are bent by combination of barrel toroid and end-cap magnets. In the barrel region, tracks are measured in chambers arranged in three cylindrical layers around the beam axis, while in the transition and end-cap regions, the chambers are installed in planes perpendicular to the beam axis, also in three layers. Over most of the η -range, a precision measurement of the track coordinates is provided by the Monitored Drift Tubes (MDT). At large pseudorapidities, the Cathode Strip Chambers (CSC) with higher granularity are used to withstand demanding rate and background conditions.

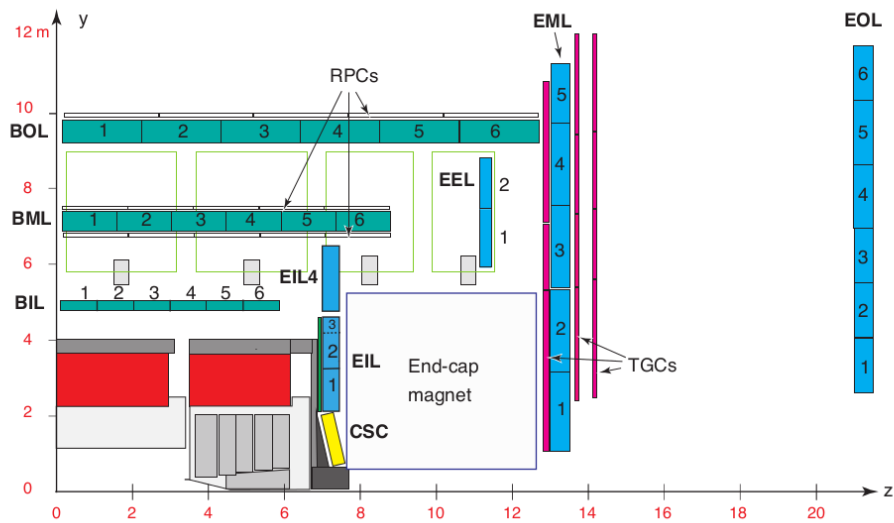


Figure 3.8: Cross-section of the quadrant of the muon system in a plane containing the beam axis. The MDT chambers in the barrel are arranged in three concentric cylindrical shells around the beam axis. In the end-cap region, muon chambers form large wheels, perpendicular to the z-axis. In the forward region, CSC is used in the innermost tracking layer. The RPC and TGC chambers are arranged in three layers (called stations) as indicated in the figure. [33]

The pseudorapidity range of $|\eta| < 2.4$ is covered by an additional trigger system which is equipped with Resistive Plate Chambers (RPC) in the barrel ($|\eta| < 1.05$) and Thin Gap Chambers (TGC) in end-cap ($1.05 < |\eta| < 2.4$) regions, respectively. The main purpose is to provide fast track information for triggering purposes with a well-defined p_T thresholds.

3.7 Forward detectors

The forward detectors are placed at high pseudorapidities and their primary objective is to measure a beam luminosity for the ATLAS detector. Furthermore, in conjunction with the main ATLAS detector body they are used to study soft QCD and diffractive physics in the initial low luminosity phase of ATLAS running. All of these detectors use different techniques to detect fragments from the collisions.

LUCID (Luminosity measurement using Čerenkov Integrating Detector) is composed of two modules located at ± 17 m from the interaction point that provide a coverage $5.5 < |\eta| < 5.9$ for charged particles. Each arm is equipped with 20 projective aluminum tubes filled with C_4F_{10} gas pointing towards interaction point and detection mechanism is based on Cherenkov radiation. The main intent of LUCID is to measure ATLAS luminosity using the inelastic collision products with sufficient efficiency and low sensitivity to the background. [38]

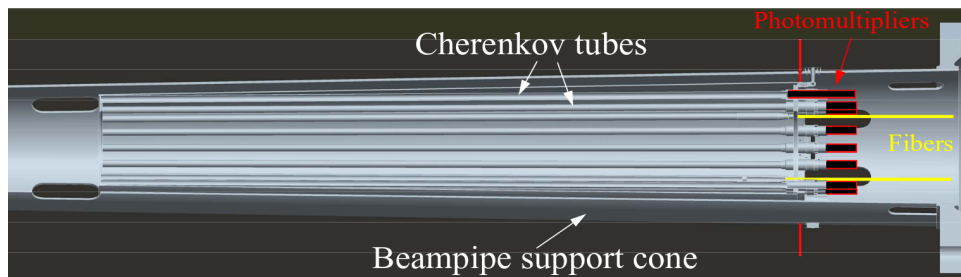


Figure 3.9: Schematics of LUCID detector based on Cherenkov radiation. [39]

ZDC (Zero Degree Calorimeter) provides coverage of the region $|\eta| > 8.3$ for neutral particles and is placed 140 m from the interaction point. The ZDC plays important role in the heavy ion physics program at the LHC. The ZDC is a sampling calorimeter that uses Cherenkov light detection produced by the highly energetic charged particles in the shower. The active element is made of quartz rods and the light produced in the rods is detected by photomultipliers. As an absorber, the tungsten plates are used. [40]

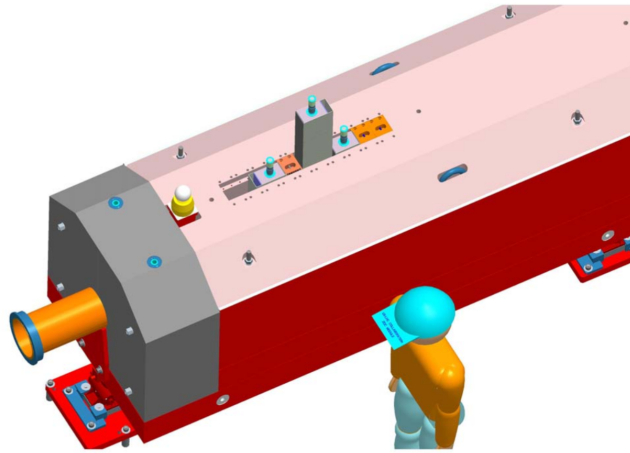


Figure 3.10: Schematics of ATLAS ZDC detector used for luminosity measurement and Heavy ion program. [39]

ALFA (Absolute Luminosity For ATLAS) is located at ± 240 m from the interaction point. The whole detector is placed in the specialized retractable devices called Roman pots which allows to have the detector in the primary vacuum of the LHC. At the beginning of the run, the ALFA detectors are in withdrawn position far from the beam. After the beam has stabilized, the detectors are moved back to within 1.5 mm of the beam. The scintillating fibers are used for detection of elastic and diffractive protons deflected from the beam [41].

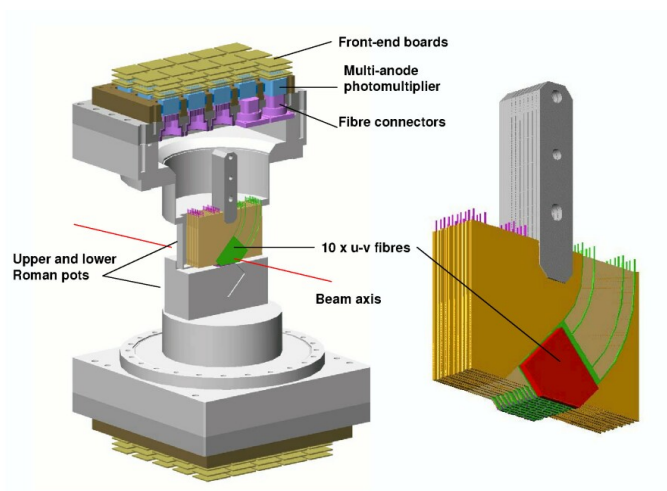


Figure 3.11: Schematics of ALFA detector and special retractable devices called Roman pots. [39]

Chapter 4

Data analysis

4.1 Data acquisition and processing

The data used in this analysis were taken during LHC Run-2 during periods D through J in proton-proton collisions at 13 TeV, where only the data collected with a stable beam operation are used. The criteria of quality were applied at the luminosity block levels. ¹

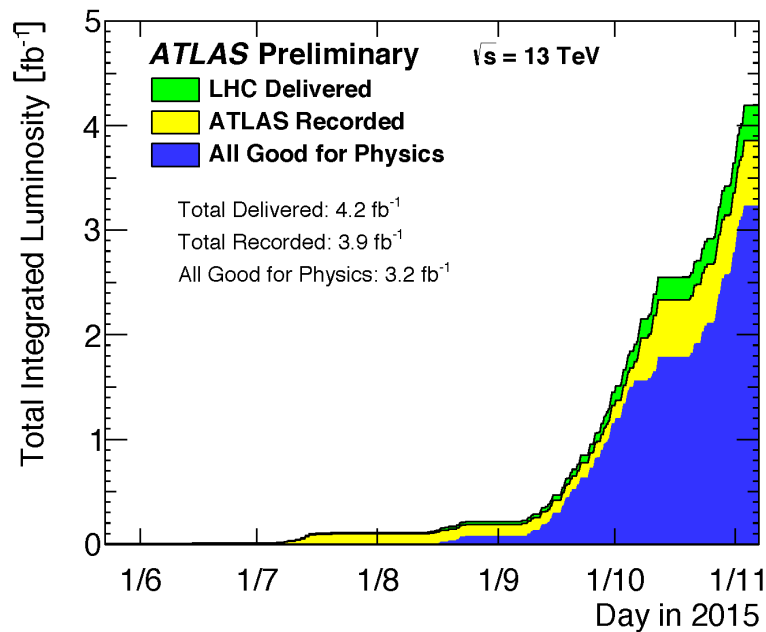


Figure 4.1: Cumulative luminosity versus time delivered to ATLAS (green), recorded by ATLAS (yellow), and certified to be good quality data (blue) during stable beams for pp collisions at 13 TeV centre-of-mass energy in 2015. [42]

¹The luminosity block is an atomic unit of the ATLAS data, which lasts 60 seconds.

To ensure the quality criteria, the collected data are filtered by a Good Runs List (GRL). The GRL selects only those events, where all detectors worked properly and are tagged as good for physics. Based on the GRL, the luminosity was calculated using the `ilumicalc` [43] tool which take in account the prescale levels and triggers dead time. The integrated luminosity of samples after trigger pass is 1.84 fb^{-1} .

4.2 Pile-up

Pile-up is phenomena, when is in the detector information from two different events or collisions detected at the same time. This is a complication for reconstruction algorithms which are trying to get right information about the event and decide if the particle belongs to the event. We distinguish two sources of pile-up:

- in-time pile-up which results from multiple interactions in the same bunch crossing
- out-of-time pile-up refers to overlapping of the read-out window with interactions from adjacent bunch crossings.

In figure 4.2 can be seen that mean number of interactions per bunch crossing in 2015 is $\langle \mu \rangle = 13.5$ for 25 ns bunch spacing and $\mu = 19.6$ for 50 ns bunch spacing.

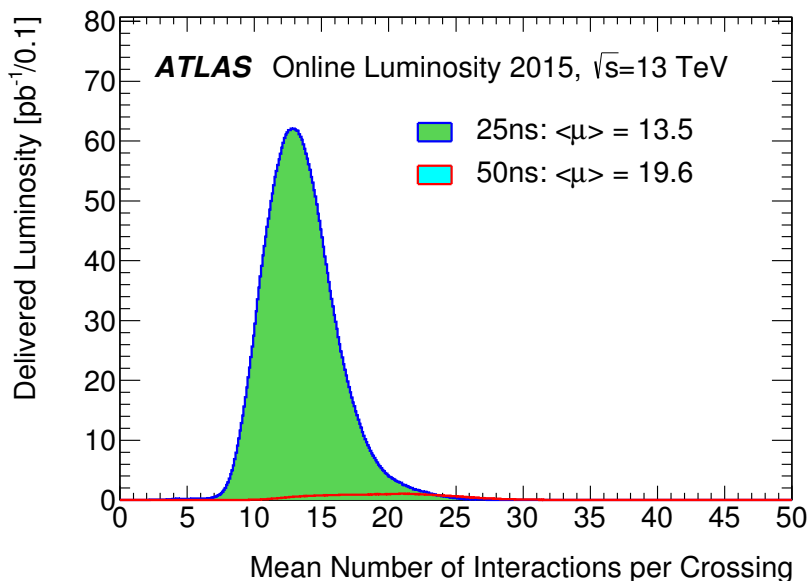


Figure 4.2: The luminosity-weighted distribution of the mean number of interactions per crossing for the 2015 pp collision data recorded from 3 June - 3 November at 13 TeV centre-of-mass energy. [42]

4.3 Trigger system

The trigger system evaluates according to certain predefined physics signatures which collision events should be saved to disk for further analysis. At the conditions which prevail on the LHC, the trigger system has to be sophisticated enough to select only the events which are physically interesting, such as events with high p_T objects of missing E_T and reduce the flux of information. The trigger system is designed to reduce the event rate from the design bunch-crossing rate of 40 MHz to an average recording rate of a few hundred Hz.

The ATLAS detector was using a three-level trigger system, for Run-2 there a different trigger scheme was devised. The new trigger system consists of a hardware Level-1 (L1) and a software-based high-level trigger (HLT). This new trigger system is faster than the previous one and saves computing resources.

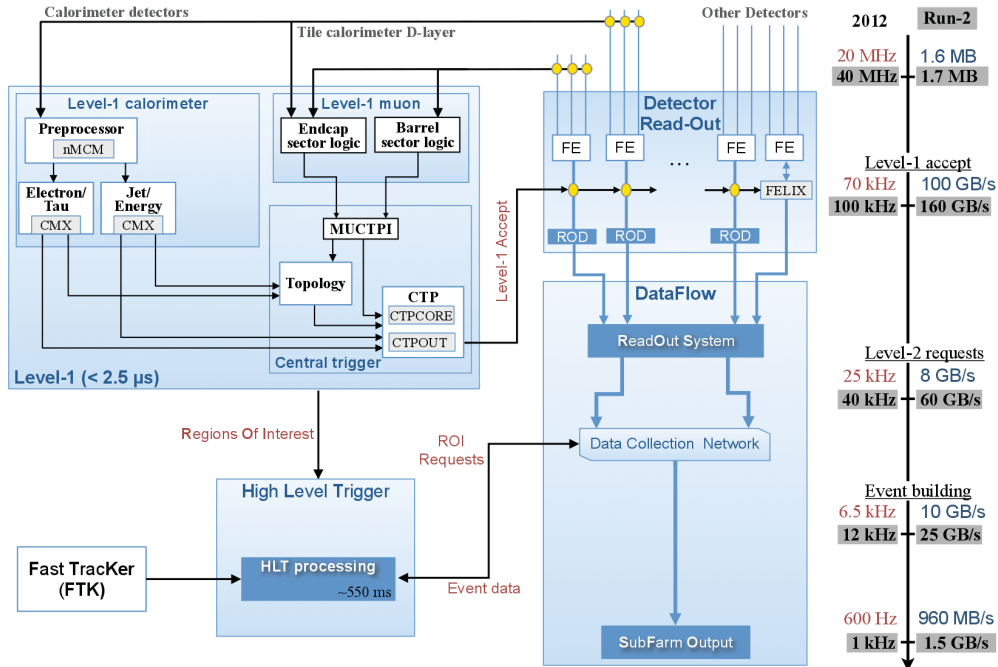


Figure 4.3: Schematic overview of the Run-2 configuration of the Trigger and DAQ system. [44]

Level-1 trigger is hardware based trigger which uses information from the fast detectors such as RPCs or TGCs for muon chambers and LAr ECAL and TileCal for calorimetric cluster information. The L1 trigger operates with rough detector position (ϕ , θ) information also called RoIs², region of interest and decide if the event will be investigated by the higher trigger level. The L1

²RoI... region of interests are detector area, where the Level-trigger sees the interesting detector signature and tag them for further processing

has only 2.5 μs to decide. There is no tracking information extracted from the ID because the readout system is not fast enough to get all information.

HLT trigger is a software based trigger running on the computer farms which use Linux operating system. The HLT, receives data at full granularity within the RoI provided by the LVL1 and combines information from all detectors, pixels including. After that, the system decides whether the event will be written on to the data storage medium.

4.3.1 Trigger menu

The ATLAS detector employs many different types of triggers. Each trigger is developed for specific a purpose. The list of trigger algorithms used for data-taking is called trigger menu. The triggers in the trigger menu can be divided to following categories: primary triggers (also called physics triggers), support triggers used for efficiency and performance measurements or monitoring, alternative triggers, backup triggers and calibration triggers.

The output from the trigger algorithms is organized into streams. Physics analysis streams require full detector information, while monitoring and calibration streams focus on a specific data subset or detector region. The data used for the purpose of this analysis are based on the B-physics stream with Level-1 rate 8 kHz and HLT rate 52 Hz.

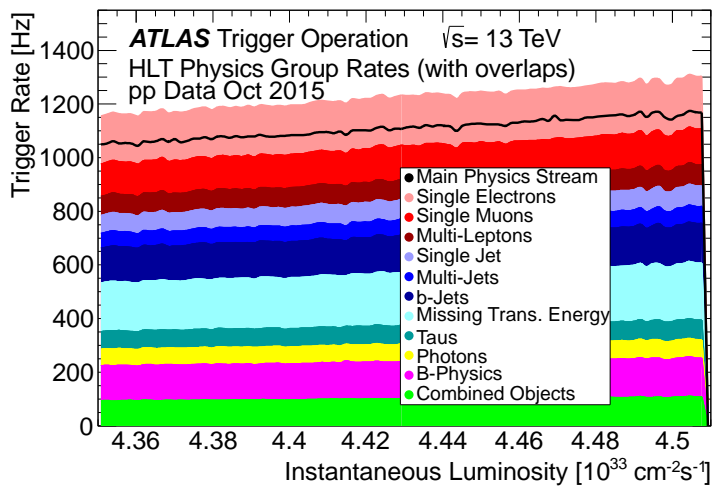


Figure 4.4: Physics trigger group rates at the High Level Trigger as a function of the instantaneous luminosity in a fill taken in October 2015 with a peak luminosity of $\mathcal{L} = 4.6 \times 10^{33} \text{ cm}^{-2} \text{ s}^{-1}$ and an average pile up of $\langle \mu \rangle = 15$. [45]

4.3.2 B-physics trigger

Trigger selection of events for physics studies of B-meson decays (B-physics triggers) is mostly based on identification of B-hadrons through their decay chains with a muon pair in the final state. The di-muon triggers require two muons at Level-1 with p_T higher than 4 or 6 GeV and pseudorapidity $|\eta| < 2.3$. The rate of di-muon triggers is reduced compared to single-muon Level-1 items, however at high transverse momentum, where the two muons become close in opening angle for low-mass resonances, the Level-1 fails to build separate RoIs.

If the event pass the Level-1 trigger, the muons are reconstructed using identical HLT algorithms as in the muon-trigger items, with the additional requirements that the two muons should form a good vertex within a certain invariant mass window [46].

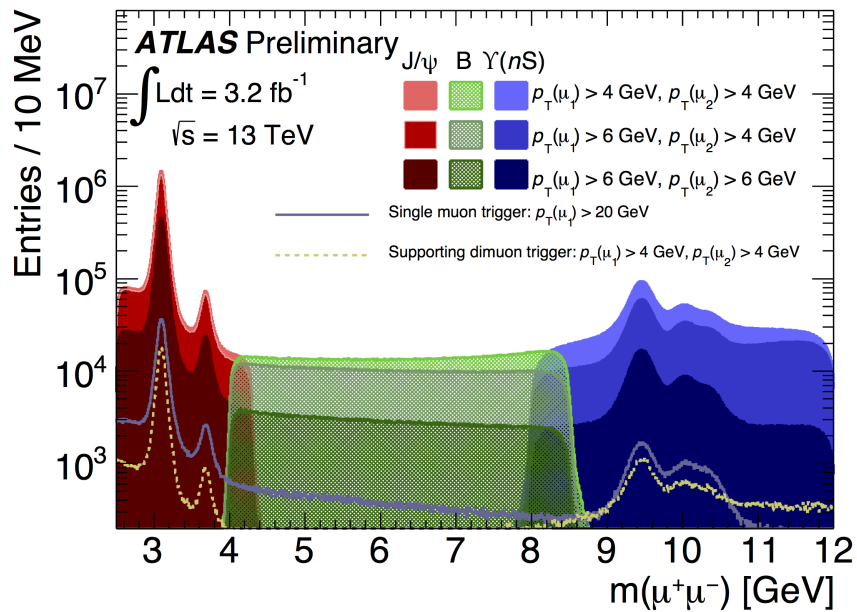


Figure 4.5: Invariant mass distributions for oppositely charged muon candidate pairs that pass various triggers. [47]

Additional primary and supporting triggers are also implemented. Triggers are based on the single Level-1 muon RoIs with an additional track found at the HLT. These triggers do not suffer with similar opening angle issues, but due to high rate they need to be highly prescaled³.

4.4 ATLAS software

The analysis presented in this thesis was implemented in C++ and ROOT [48] with usage of RootCore and RooFit [49] frameworks. The whole analysis process is divided into smaller macros,

³The prescale is reducing the effective yield of events collected by the triggers.

each committed to one specific purpose. These macros are connected using Python scripts which provide communication and smooth running of the analysis. The RAW data reconstruction is performed in the Athena software framework [50], which can be also used alternatively for physics analysis.

ROOT is an object oriented analysis tool for data processing developed at CERN and is available under the LGPL license. ROOT uses C++ syntax and provides an advanced statistical analysis and visualization tools. The ROOT framework provides containment for analysis processing and storage of analysis results in the proprietary ROOT tree structure. It also allows usage of parallel computing tools for effective processing of large data files. The analysis presented here is processed using the ROOT version 6.02/12.

RooFit packages provides a toolkit for modeling the expected distribution of events in a physics analysis. Models can be used to perform likelihood fits, produce plots, and generate "toy Monte Carlo"⁴ samples for various studies. The RooFit tools are integrated with the object-oriented and interactive ROOT graphical environment.

RootCore is the high-level analysis framework for the ATLAS data, providing the reconstructed data in a structured format and performance tools for the physics analyses.

Athena is a common framework for detector performance and physics studies. It is based on C++ and Python and is used to data reconstruction.

4.5 Monte Carlo simulation

Monte Carlo event generators are used extensively in collider physics. Pythia8 [51] is one of the most commonly used generator, using the parton shower approach. The parton shower approach is based on the assumption that a $2 \rightarrow n$ process, with a complex final state is achieved by starting from a simple $2 \rightarrow 2$ process, which is called parton shower approximation.

In order to generate the final state, Pythia has to perform several steps. First, two particles from the incoming beams are coming upon each other. Normally, each proton is characterized by a set of parton distributions, which define the partonic substructure. After that, one shower initiator parton from each beam starts off a sequence of branchings, such as $q \rightarrow qg$, which build up an initial-state shower. One incoming parton from each of the two showers enters the hard process. These hard processes described by QCD are calculated using perturbation theory, most commonly in leading order. In next step, there follows the generation of all subsequent activity on the partonic level, involving final-state radiation, multiple parton-parton interactions and the

⁴Toy Monte Carlo is method based on the random generators using simplified model used to reproduce the more complex physics problem.

structure of beam remnants. In the final step, hadronisation of this final parton configuration, followed by the decays of unstable particles. [51]

To obtain full detector simulation of these events, the Geant4⁵ suite is used. The Geant4 simulates the passage of the generated particles through the detector and output data are reconstructed with the same algorithms that are used to process the data from the detector. The ATLAS Geant4 simulation contains over the million volumes including the active and inactive material to describe the ATLAS geometry.

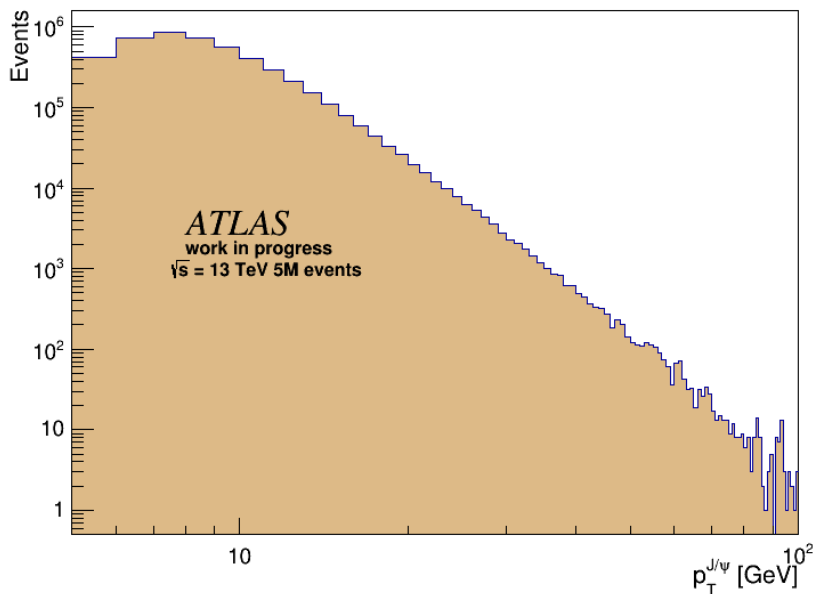


Figure 4.6: The distribution of J/ψ p_T of the Monte Carlo data sample.

4.5.1 Monte Carlo data

The analysis presented here uses MC process $pp \rightarrow J/\psi \rightarrow \mu^+\mu^-$ with CTEQ6L1 parton distributions, where the minimum p_T of decay muon is 2.5 GeV. The data sample⁶ it has 5M events with approximate cross section of 209 nb. The data sample is relatively small and suffers with low statistics in high p_T region. In order to perform more precise measurement, the MC data sample will be required.

⁵Geant4 is a toolkit for simulating the passage of particles through matter. It includes a complete range of functionality including tracking, geometry, physics models and hit generation. [52]

⁶mc15_13TeV.300000.Pythia8BPhotospp_A14_CTEQ6L1_pp_Jpsimu2p5mu2p5.merge.DAOD_BPHY1.e3989_a766_a807_r6282_p2530

4.6 Analysis Event Data Model

The first data-taking run (Run 1) of the ATLAS experiment used complicated Event Data Model (EDM), and even though it was very successful, for the Run 2 the EDM underwent substantial changes. One of the large disadvantage of the EDM from Run 1 was that the event data could not be easily converted directly into ROOT format. Additionally, ATLAS needs some kind of robust, flexible data-reduction framework to reduce required disk space. To deal with this, ATLAS converted on output the complex transient data model to a simpler persistent data model which could be written to ROOT directly. This new ATLAS event data model for analysis is called the xAOD. [53]

When the RAW data are reconstructed by the Tier-0 using the Athena tool, the output is written into the new xAOD format. At this point, one can produce final analysis n-tuples, using both Athena and ROOT, or use derivation framework to produce skimmed/slimmed xAOD. The physics analysis is usually performed on the final n-tuples. The figure 4.7 visualizes the flow of the data.

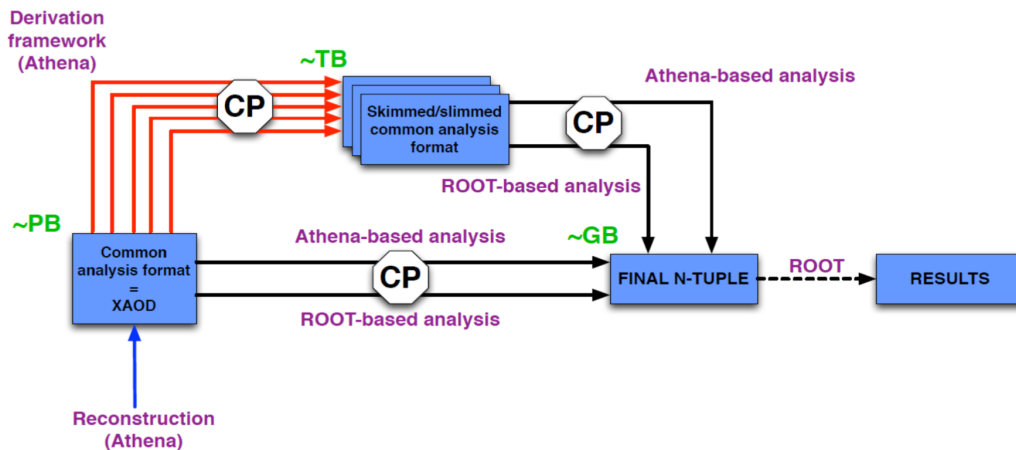


Figure 4.7: The ATLAS Run-2 analysis model consists of a new EDM (xAOD) and a centralized data-reduction framework (Derivation Framework). [53]

4.7 Event reconstruction

To measure the J/ψ production cross section, the di-muon channel was chosen, because the muons have a clean detector signature. To reconstruct muon tracks, several different strategies have been developed using physics signatures in the inner detector, calorimeters and muon detector system. Muons can be classified into four categories according to the signatures left in the detector:

- *Standalone* muons are identified using only Muon Spectrometer. The tracks are extrapolated

to the beam region to give the track parameters. Due to the position and momentum resolution of the muon chambers, their parameters are not measured as precisely as in other muon reconstruction types, but provide muons from higher pseudorapidity $|\eta| > 2.7$.

- *Combined* muons are formed by matching the Inner Detector track to the Muon Spectrometer track. The reconstruction algorithm used to identify combined muons is called *Chain 3* [54]. The combined muons have the most precisely measured parameters.
- *Tagged* muons are the ID tracks matched to the hits in the muon segments in the Muon Spectrometer. There are two tagging algorithms, MuTag [55] and MuGirl, propagating all inner detector tracks with a sufficient momentum out to the first station of the muon spectrometer and search for nearby segments.
- *Calorimeter tagged* muons use information about energy deposit in the calorimetry system matched to the ID tracks. The calorimeter muons have lower purity and efficiency than the muons reconstructed in the muon system.

To guarantee the purity of the signal, only combined muons are used to reconstruct di-muon candidates in this analysis. For the needs of B-physics working group, the special algorithm for reconstruction of dimuon candidates, called JpsiFinder, was developed. This algorithm pass through all of the muon combinations in an event, it performs a vertex fit on a pair of muons and if the dimuon pair pass all criteria, it is stored as a dimuon candidate.

4.8 Event selection

The J/ψ candidates have to be triggered by the J/ψ dimuon trigger, which requires two oppositely charged muons with $p_T > 4$ GeV. In addition they have to pass multiple selection criteria. First reconstructed candidate must fit within $|\eta| < 2.5$ and dimuon invariant mass window of 2.6–3.6 GeV. Both off-line reconstructed muons are restricted to $p_T > 4$ GeV and $|\eta| < 2.5$. To ensure high purity of the signal each track is required to have at least one Pixel hit, five SCT hits and in case the track is within $0.1 < |\eta| < 1.9$ at least six TRT hits. There can be at most 2 missing hits in the Pixel and SCT layers. For TRT hits, there is additional condition to have at least 90% of hits over outliers. The muon candidates must be matched within a cone $\Delta R = \sqrt{(\Delta\eta)^2 + (\Delta\Phi)^2} < 0.01$ between each reconstructed muon candidate and the trigger identified candidate. This last constraint rejects about 5% of candidates, but ensures that the trigger was fired by a measured muon and so the trigger unfolding can be performed.

4.9 Analysis prerequisites

The analysis presented in this thesis follow the procedure used in J/ψ cross section measurement in Run 1 [56]. The measurement is performed in several intervals of dimuon transverse momentum and absolute value of rapidity. The dimuon p_T range is restricted by kinematics conditions of $p_T(\mu\mu) > 8 \text{ GeV}$. The condition of sufficient statistics sets upper limit to $p_T < 100 \text{ GeV}$.

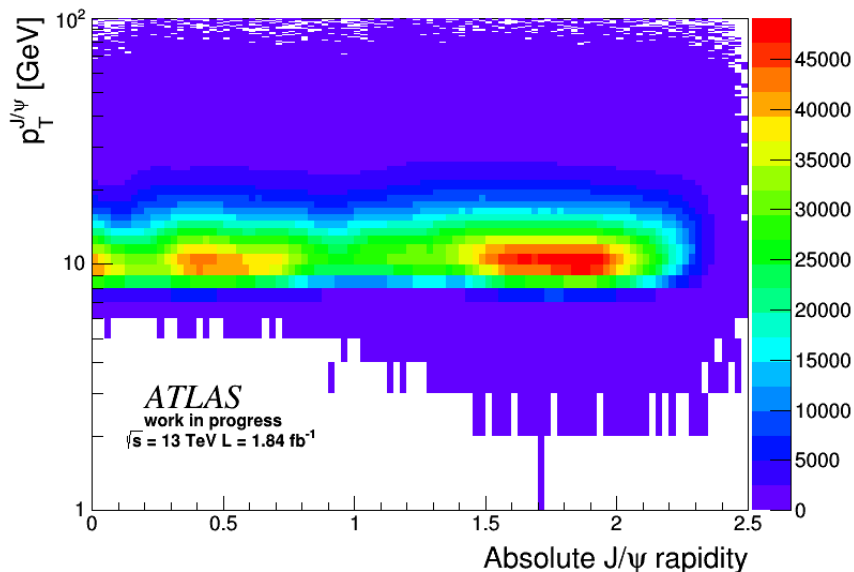


Figure 4.8: The distribution J/ψ candidates as a function of p_T and rapidity.

The measurement differs two compounds of signal prompt and non-prompt for J/ψ . The definition of prompt refers to the J/ψ states produced from short-lived QCD sources, this includes directly produced J/ψ in pp collision or indirectly produced J/ψ from feed-down from other charmonium states. If the decay chain includes long-lived, particles such as B-hadrons, then the J/ψ is labeled as non-prompt.

4.9.1 Fiducial $J/\psi \rightarrow \mu^+ \mu^-$ differential production cross section

Differential dimuon cross section in each bin for both prompt and non-prompt J/ψ is defined as

$$\frac{d^2\sigma(pp \rightarrow X \rightarrow J/\psi)}{dp_T dy} Br(J/\psi \rightarrow \mu^+ \mu^-) = \frac{N_{corr}^{p,np}}{\Delta p_T \Delta y \cdot \mathcal{L}}, \quad (4.1)$$

where Δp_T and Δy are bin widths, \mathcal{L} is the integrated luminosity of the data sample and $N_{corr}^{p,np}$ is the number of dimuon signals for each $p_T - y$ bin after background subtraction and corrected for detector inefficiencies for both prompt and non-prompt contributions. To determine the true

number of J/ψ each recorded event is weighted by a weight w . The weight w is defined as

$$w^{-1} = \mathcal{A} \cdot \mathcal{E}_{reco} \cdot \mathcal{E}_{trig}, \quad (4.2)$$

where \mathcal{E}_{reco} is the muon off-line reconstruction efficiency, \mathcal{E}_{trig} is the trigger efficiency and \mathcal{A} is the kinematic acceptance.

4.9.2 Non-prompt fraction

The pseudo-proper lifetime τ is used as a discrimination variable to identify non-prompt fraction of J/ψ candidates. The pseudo-proper lifetime is defined as lifetime in transverse plane, described by the following equation:

$$\tau = \frac{L_{xy} \cdot m_{PDG}^{J/\psi}}{p_T^{J/\psi}}, \quad (4.3)$$

where L_{xy} is distance of J/ψ vertex from primary vertex measured in the transverse plane, the $m_{PDG}^{J/\psi}$ and $p_T^{J/\psi}$ are invariant mass resp. transverse momentum of the candidate. The PDG value of world average invariant mass of J/ψ is used to reduce correlation between the invariant mass and lifetime.

Furthermore, the non-prompt fraction is defined as number of non-prompt dimuons relative to the inclusively produced dimuons:

$$f_B = \frac{pp \rightarrow b + X \rightarrow J/\psi + X'}{pp \xrightarrow{\text{Inclusive}} J/\psi + X''}. \quad (4.4)$$

4.9.3 Reconstruction and trigger efficiency

The reconstruction efficiency \mathcal{E}_{reco} for a given J/ψ candidate is calculated from single muon reconstruction efficiencies $\mathcal{E}_\mu^\pm(p_T^\pm, \eta^\pm)$ as follows:

$$\mathcal{E}_{reco} = \mathcal{E}_\mu^+(p_T^+, \eta^+) \cdot \mathcal{E}_\mu^-(p_T^-, \eta^-). \quad (4.5)$$

The off-line single muon reconstruction efficiencies are determined from tag-and-probe⁷ study in dimuon decays, and are a function of $p_T(\mu)$ and $q \times \eta(\mu)$, where q is a charge of the muon. As can be seen in figure 4.10, the reconstruction efficiency in the central region around $\eta = 0$ is significantly reduced. This low efficiency is caused by the support infrastructure and wiring of detectors located in this area.

Similar to the reconstruction efficiency, the trigger efficiency \mathcal{E}_{trig} for a given J/ψ is calculated from single muon efficiencies $\mathcal{E}_{RoI}^\pm(p_T^\pm, q, \eta^\pm)$. An additional correction factor $c_{\mu\mu}(\Delta R, |y^{\mu\mu}|)$ is applied to account for dimuon effects such as overlapping RoIs or vertex quality. The trigger

⁷Tag-and-probe is method developed to measure the efficiency of particular cut or trigger, this method is detailed described in [57].

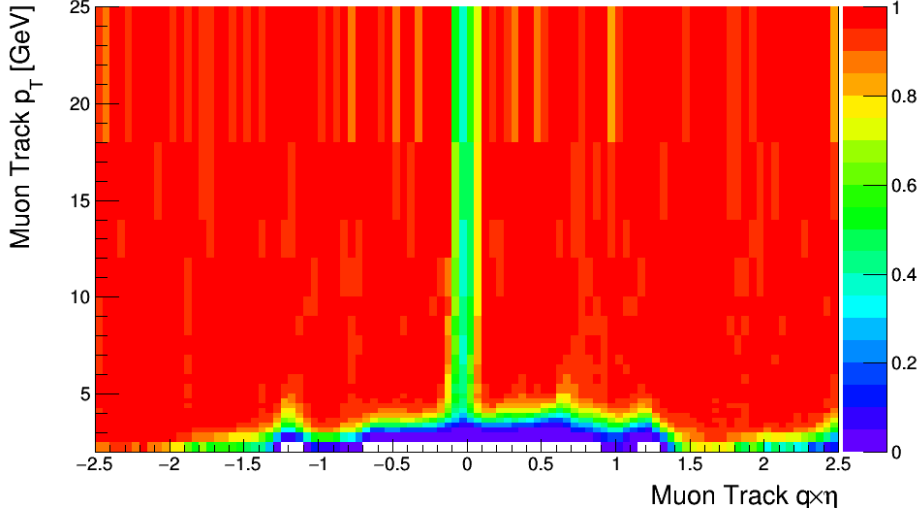


Figure 4.9: The muon offline reconstruction efficiency map for 13 TeV data as a function of the muon charge-signed pseudorapidity and muon p_T . [58]

efficiency is then computed as

$$\mathcal{E}_{trig} = \mathcal{E}_{RoI}^+(p_T^+, q, \eta^+) \cdot \mathcal{E}_{RoI}^-(p_T^-, q, \eta^-) \cdot c_{\mu\mu}(\Delta R, |y^{\mu\mu}|). \quad (4.6)$$

$C_{\mu\mu}$ correction factor, extracted using tag-and-probe method, is divided in three bins of rapidity. The muon triggered by the HLT_mu4_bJpsi_Trkloose trigger was used as tag muon and the muon which fire the HLT_2mu4_bJpsimumu trigger as a probe. The HLT_mu4_bJpsi_Trkloose trigger is based on L1-mu4 trigger which requires single muon with p_T higher than 4 GeV and at HLT level it requires muon plus track coming from the same vertex. The trigger with same cut on p_T was used to avoid bias in the low p_T region.

4.9.4 Acceptance

The kinematic acceptance $\mathcal{A}(p_T, y)$ is the probability that the muons from J/ψ decay with rapidity y and transverse momentum p_T fall into fiducial volume of the ATLAS detector. The acceptance maps are computed using toy Monte Carlo generator applying selection criteria on particle momenta and rapidity to emulate the detector geometry. The final acceptance map for isotropic distribution is presented in the figure 4.11.

The acceptance also depends on spin alignment of J/ψ production mechanism, which is not well known for current LHC conditions. This affects angular distribution of dimuon decays. The

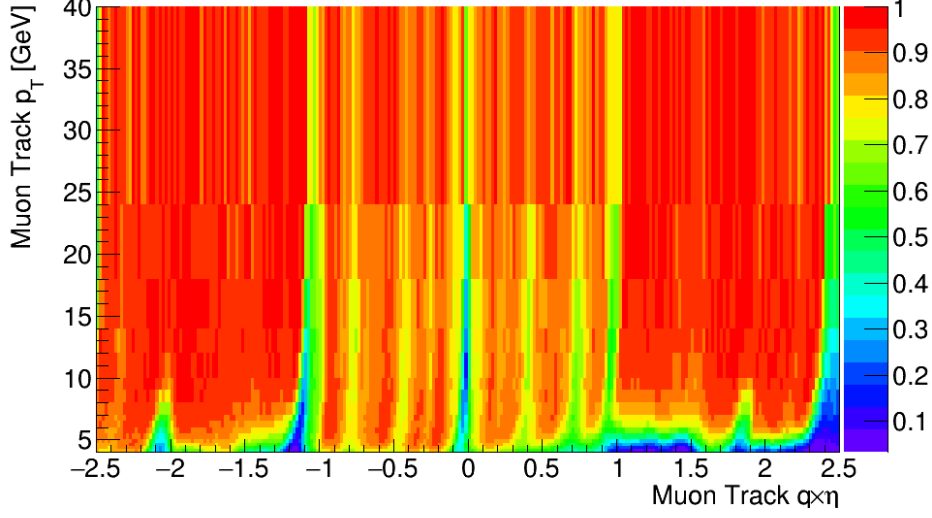


Figure 4.10: The single muon trigger efficiency map of HLT_2mu4_bJpsimumu trigger for 13 TeV data as a function of the muon charge-signed pseudorapidity and muon p_T . [58]

general decay frame of J/ψ candidate is given by the following relation:

$$\frac{d^2N}{d \cos \theta^* d \phi^*} \propto 1 + \lambda_\theta \cos^2 \theta^* + \lambda_\phi \sin^2 \theta^* \cos 2\phi^* + \lambda_{\theta\phi} \sin 2\theta^* \cos \phi^*, \quad (4.7)$$

where the θ^* is the angle between the direction of the positive muon momentum in the J/ψ decay frame and the J/ψ line of flight. The ϕ^* is the angle between the J/ψ production and decay planes in the lab frame.

The different production scenarios were studied, such as longitudinal polarization where $\lambda_\theta = -1$, $\lambda_\phi = \lambda_{\phi\theta} = 0$ or transverse alignment where $\lambda_\theta = +1$, $\lambda_\phi = \lambda_{\phi\theta} = 0$ etc., but for the main polarization scenario isotropic distribution independent on θ^* and ϕ^* is used with $\lambda_\theta = \lambda_\phi = \lambda_{\phi\theta} = 0$. Using isotropic distribution, the angular distribution will correspond to the detector effects only.

4.10 Fitting procedure

Two-dimensional unbinned maximum likelihood fit of weighted events was made in each bin of p_T and $|y|$. The each bin was fitted separately with its own sets of parameters. The fit consists of prompt and non-prompt contributions of J/ψ , and three sets of background functions.

The final likelihood function takes following form:

$$\mathcal{L} = \sum_{i=1}^5 f_i \cdot P_i(m, \tau) \otimes R(\tau), \quad (4.8)$$

Unpolarised

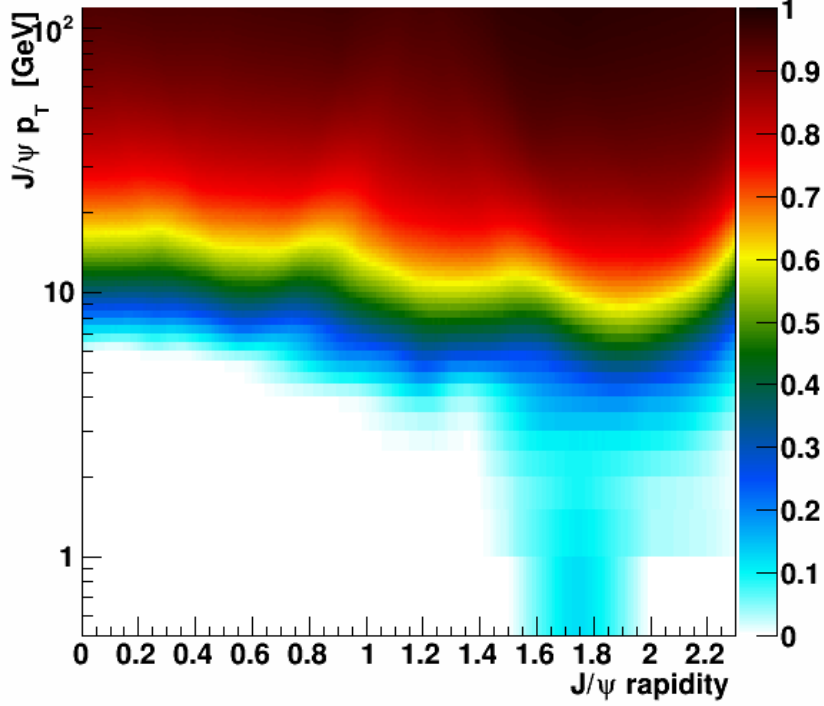


Figure 4.11: The acceptance map of unpolarized J/ψ hypothesis, shown as a function of the p_T and rapidity.

where f_i is the normalization factor, $P_i(m, \tau)$ is two-dimensional probability function for all contributions and $R(\tau)$ is the resolution term common for all pseudo-proper lifetime distributions.

For the description of the both prompt and non-prompt signal in the invariant mass frame the Crystal Ball [59] distribution was used. In the pseudo-proper time frame, the dirac function convolved with the resolution function for prompt and one-sided exponential convolved with identical resolution function for non-prompt J/ψ s is used. The resolution function is then to be the gaussian distribution and the same for all pseudo-proper time distributions.

The background is composed of three components. The prompt component of background is described by the linear function in invariant mass frame and dirac function convolved with the resolution function in pseudo-proper time frame. There are two components of non-prompt background. The first one is exponential for invariant mass frame and single sided exponential convolved with the resolution function in pseudo-proper time frame. The second one is exponential for invariant mass frame and flipped single sided exponential convolved with the resolution function in pseudo-proper time frame. The negative pseudo-proper lifetime of the background is connected with miss match during reconstruction, combinatoric background and non-coherent dimuon pairs.

All of the components that contribute to the overall fit function are summarized in table 4.1.

Source	Type	invariant mass frame	pseudo-proper time frame
J/ψ	prompt	$CB(\sigma_{1p}, \mu_1, \alpha_1, n)$	$\delta(0)$
	non-prompt	$CB(\sigma_{1n}, \mu_1, \alpha_1, n)$	$E_1(\tau_1)$
Background	prompt	$L(a_1)$	$\delta(0)$
	non-prompt	$E_2(\lambda_1)$	$E_3(\tau_2)$
	non-prompt	$E_4(\lambda_2)$	$E_5(-\tau_3)$

Table 4.1: Components of the fit function. The CB means Crystal Ball distribution, E exponential, δ is dirac delta function and L is linear function. All distributions in pseudo-proper time are convolved with gaussian resolution function $G(0, \sigma)$.

From the fit results, many useful dependencies can be extracted such as J/ψ production cross section and non-prompt to prompt ratio for J/ψ meson. In this analysis, fit is used to separate only the prompt data sample for the spin alignment measurement.

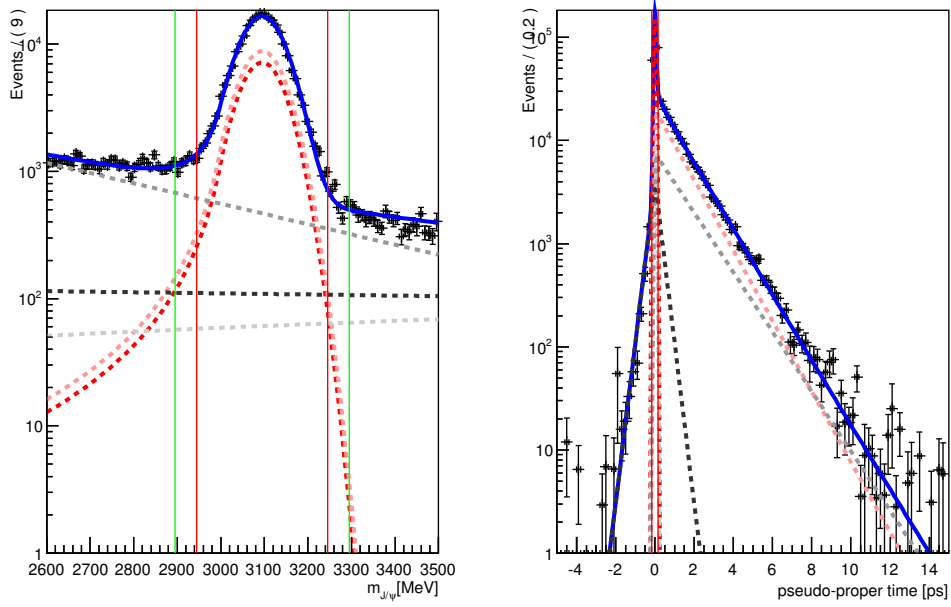


Figure 4.12: The projection of the J/ψ simultaneous mass-pseudo-proper lifetime fit result for $18 \text{ GeV} < p_T < 20 \text{ GeV}$ and $0.75 < |y| < 1.00$ bin in 13 TeV data. The invariant mass part of the projection is shown on the left side and the pseudo-proper time projection on the right side.

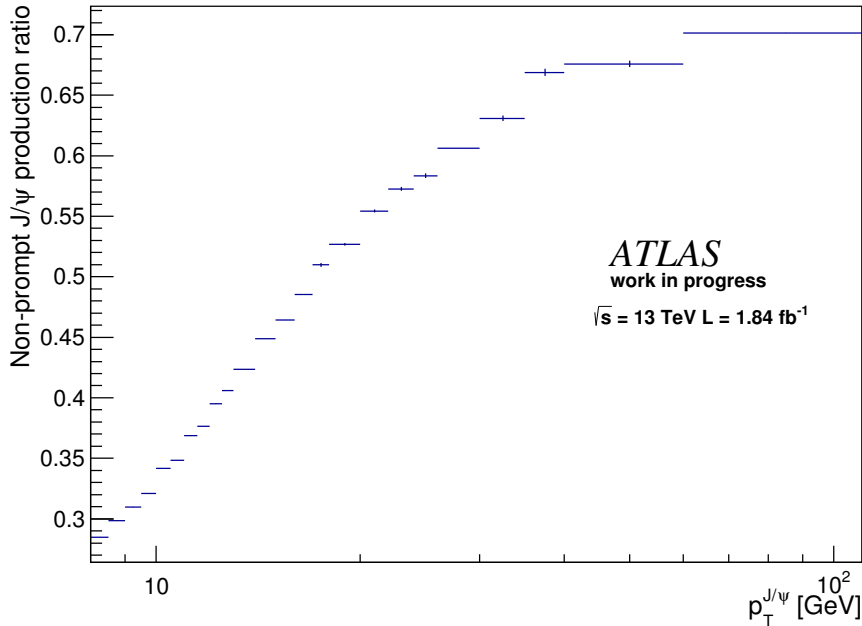


Figure 4.13: The non-prompt J/ψ fraction extracted from fit in the rapidity $0.75 < |y| < 1.00$.

4.11 Prompt J/ψ selection

As is shown in figure 4.13, the fraction of non-prompt produced J/ψ increases with p_T . Thus we have to apply additional cuts on the data sample to get only prompt events. To do so, we select only the events in $\pm 3\sigma$ from the invariant mass peak and $\pm 3\sigma$ around the pseudo-proper lifetime. This suppresses the non prompt and background events in the data sample under the level of 20%. The events in the distance larger than 4σ are in the sideband region.

Applying these cuts we get two: streams signal and background. In the first stream, the prompt J/ψ are most frequently found. The second one, the background stream where the dominant contribution is made of non-prompt J/ψ . The figure 4.15 shows the ϕ^* , $\cos\theta^*$ distribution for both streams.

In each p_T and rapidity bin, the polarization of background is subtracted from the signal region. The subtraction is made in the fraction of the background events in the signal region figure as can be seen in figure 4.14. After this step, we should be able to perform unbinned most likelihood fit of polarization template.

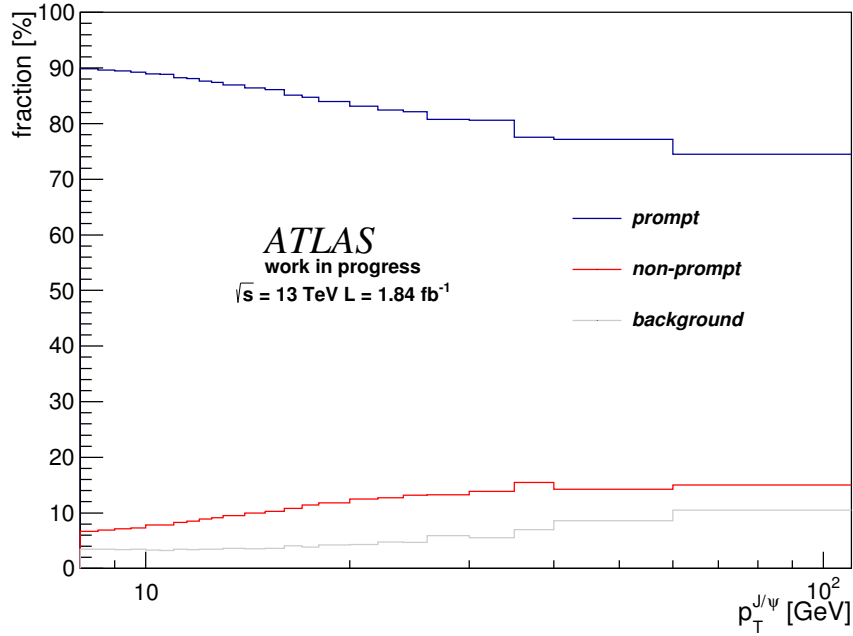


Figure 4.14: The prompt and non-prompt fractions in the data sample after the cut on the invariant mass and pseudo-proper time.

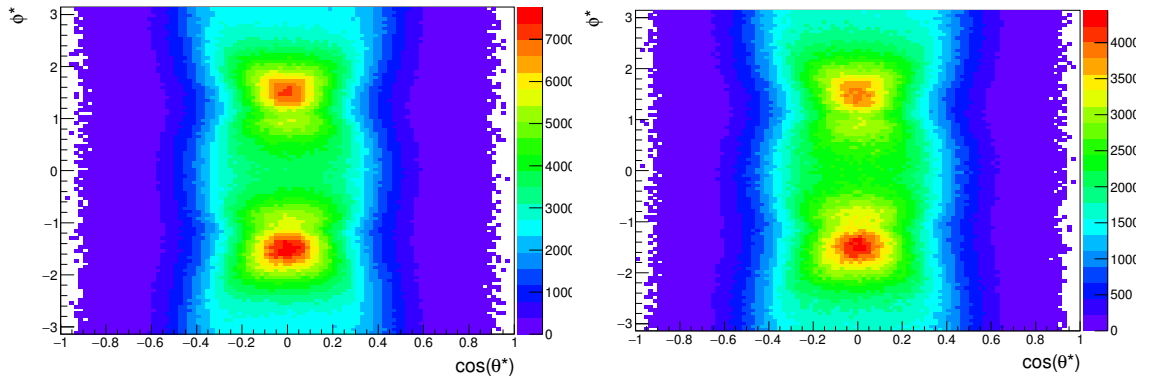


Figure 4.15: The unweighted angular distribution of decay muons for the signal region(right) and the background region (left).

4.12 Polarization template

The templates for polarization fit were produced using Monte Carlo data. The Monte Carlo generator Pythia8B was used to produce prompt J/ψ with zero polarization. Because the MC

generated events do not contain background and non-prompt J/ψ , the part of fitting procedure which subtracts background can be skipped.

The MC data were divided into the p_T with same binning as the real data and weight of each MC event is computed similar to 4.2, but did not include trigger efficiency. For each p_T bin, the $\cos\theta^*$ and ϕ^* template was produced. The figure 4.16 illustrates the MC template for selected bins.

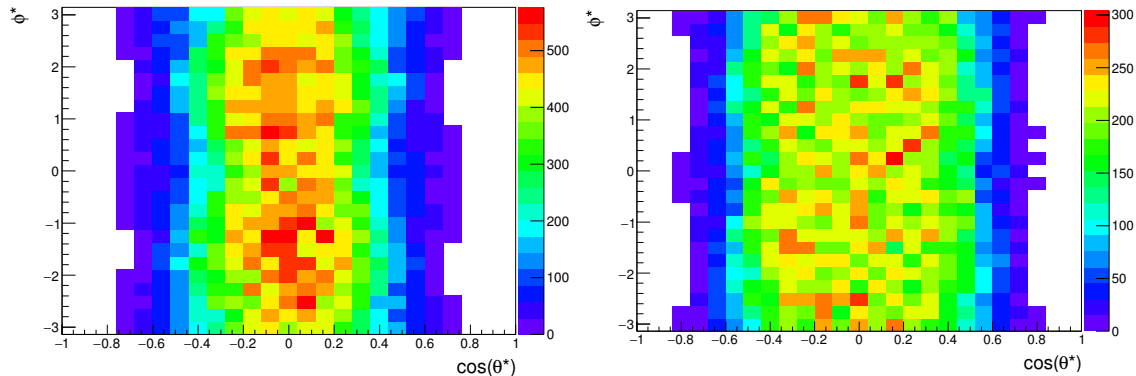


Figure 4.16: The example of weighted MC templates for the selected bins 10–10.5 GeV(left) and 13–14 GeV(right).

4.13 Polarization fit

After we obtain a clean sample of prompt J/ψ from $\sqrt{s} = 13$ TeV data and MC templates, the polarization template fit can be performed. Because the MC templates were produced only in p_T bins due to small statistics, the results from all rapidity bins are merged into one dataset and the polarization analysis is performed in p_T bins only. The model, used to fit the data, is composed of two parts: the MC template used as the skeleton for the fit and the polarization weight, which describes difference between zero polarized MC template and measured data with basic state of polarization $T^{0\pm}$. The final equation can be described as follows

$$model_i(\lambda_\theta, \lambda_\phi, \lambda_{\theta\phi}) = \omega_i(\lambda_\theta, \lambda_\phi, \lambda_{\theta\phi}) \cdot template_i \cdot N, \quad (4.9)$$

where template represents the distribution of MC data, N is event normalization and ω is the spin-alignment distribution according to the equation 2.9.

Figures 4.17 and 4.18 show the result of the polarization template fit in one lower p_T and one higher p_T region.

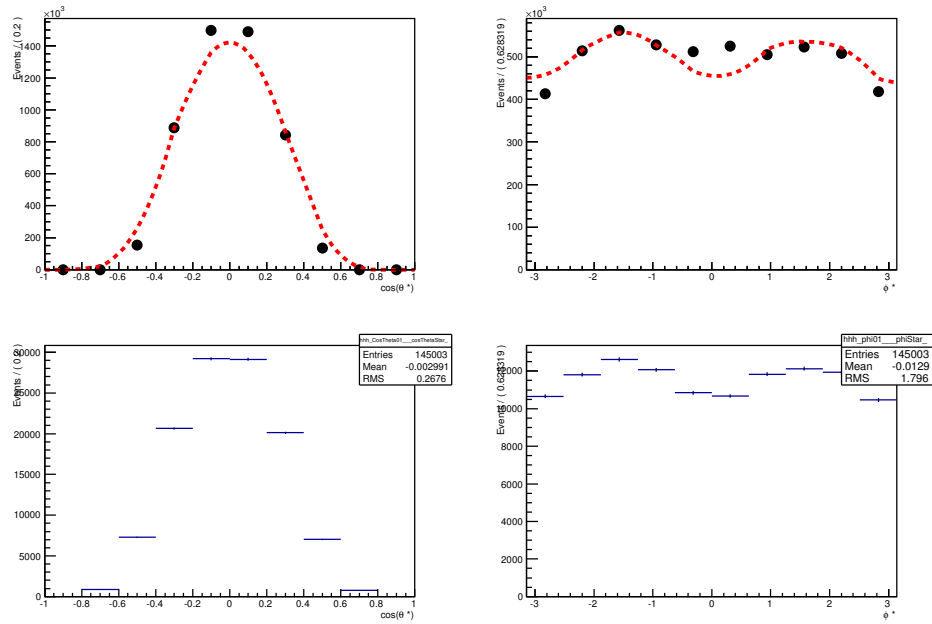


Figure 4.17: The result of polarization template fit in the $10 < p_T < 10.5$ GeV bin at the top and the projection of MC template into $\cos \theta^*$ and ϕ^* plane bottom.

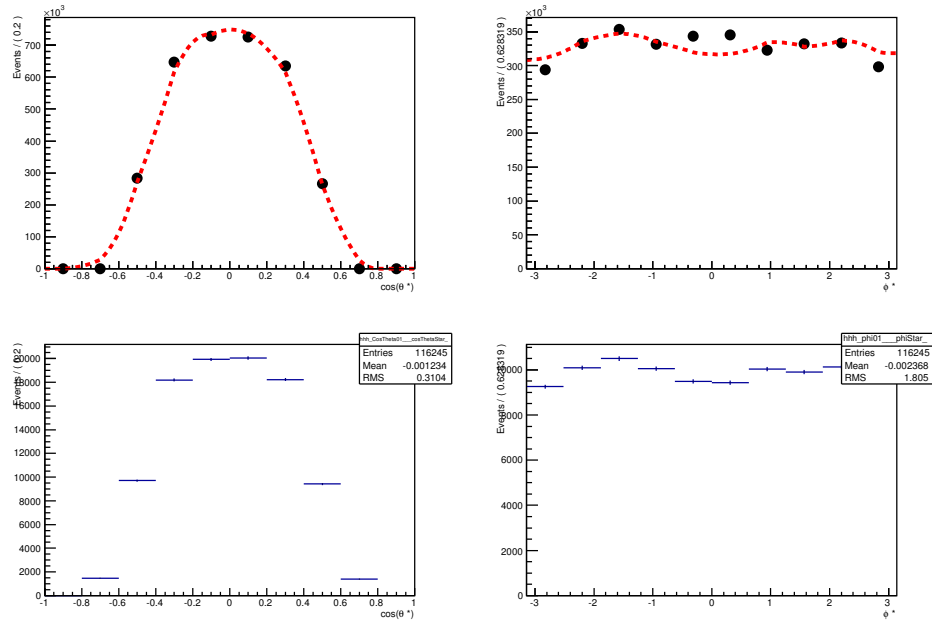


Figure 4.18: The result of polarization template fit in the $13 < p_T < 14$ GeV bin at the top and the projection of MC template into $\cos \theta^*$ and ϕ^* plane bottom.

Chapter 5

Results

The following chapter summarizes all results obtained from the simultaneous unbinned maximum likelihood fits of the data. The results from polarization template fit are also shown. The results are presented with statistical uncertainty and the systematic uncertainty computed as envelope of different spin alignment scenario only. Other systematic uncertainties are not calculated yet because the main analysis of is still in progress, but the most significant uncertainties would be originating in the trigger and reconstruction efficiencies, fit model and luminosity.

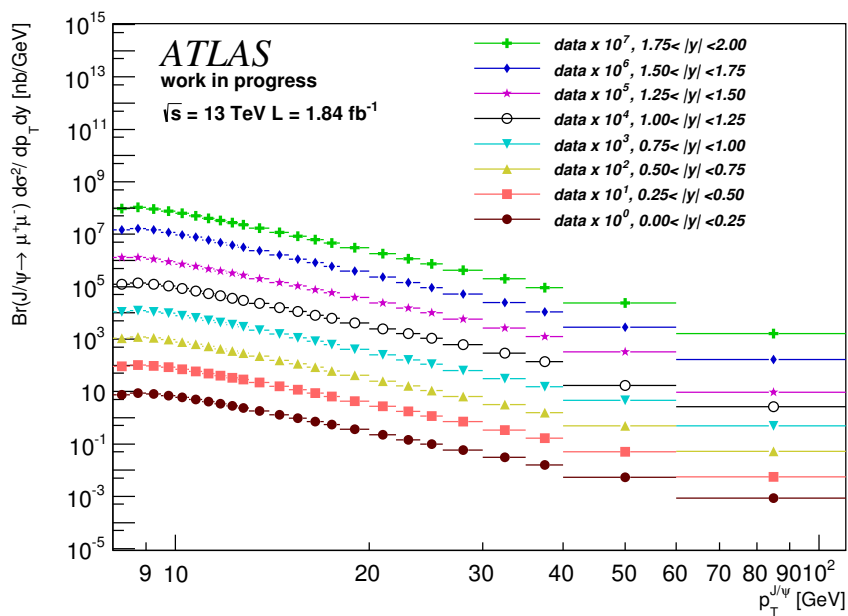


Figure 5.1: The J/ψ differential production cross-section for $\sqrt{s} = 13 \text{ TeV}$ data as a function of $J/\psi p_T$ in several bins of rapidity.

5.1 Mass lifetime fit

As it can be seen in the figures 5.1 and 5.2, the J/ψ fit results are stable over the entire range except one p_T -rapidity bin, where the fit does not converge well. This error reflects in both cross-section and non-prompt J/ψ fraction histograms and propagates further into the polarization measurement.

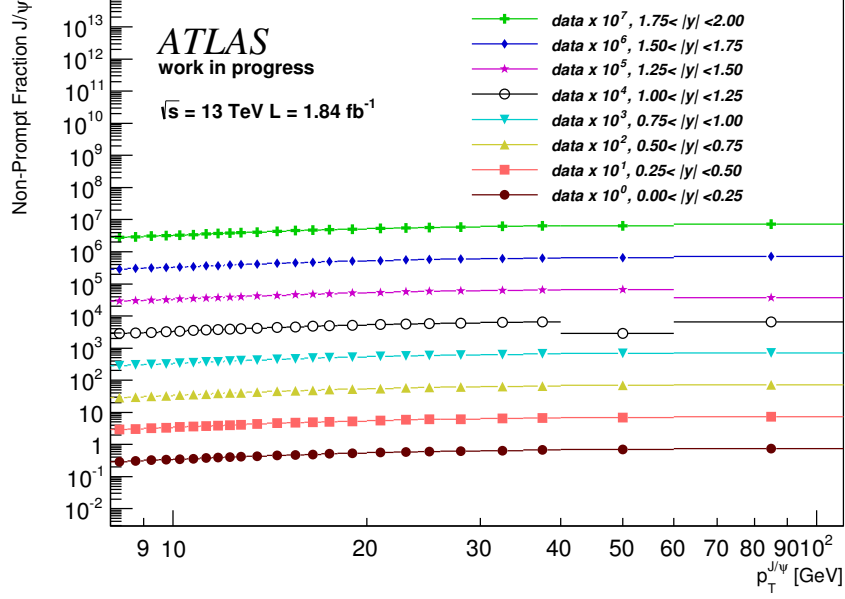


Figure 5.2: The non-prompt J/ψ production fraction for $\sqrt{s} = 13$ TeV data as a function of J/ψ p_T in several bins in rapidity.

Figure 5.3 shows the comparison of the measurement presented here at $\sqrt{s} = 13$ TeV and the official ATLAS results from Run-1 at $\sqrt{s} = 8$ TeV. As it can be seen, the obtained non-prompt fraction is little higher than the official one, but it still follows the same tendency and are compatible within the error.

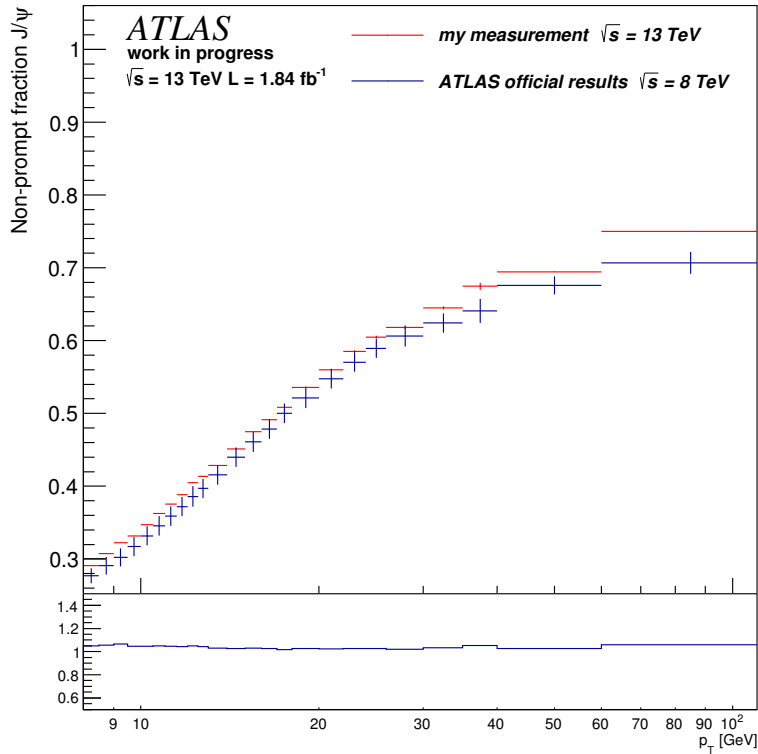


Figure 5.3: Non-prompt fraction compared to official ATLAS measurement at $\sqrt{s} = 8 \text{ TeV}$ in the rapidity bin $|y| < 0.25$.

5.2 Polarization fit

The result of polarization parameters λ are summarized in the figures 5.4, 5.5 and 5.6. The polarization fit is much less stable than the mass lifetime fit, mainly because of the small statistics of MC sample. In figure 5.4 it can be seen that in low p_T bins the polarization template fit have problems to converge and the error of fit results in these bins is orders of magnitude larger than in the other bins. This is probably caused by low efficiency of used trigger and because the trigger efficiency maps are still preliminary the correction may change. Looking at the preliminary fit results, it favor an isotropic spin alignment of prompt J/ψ , but without final efficiency maps the result is incomplete and the final polarization can significantly change.

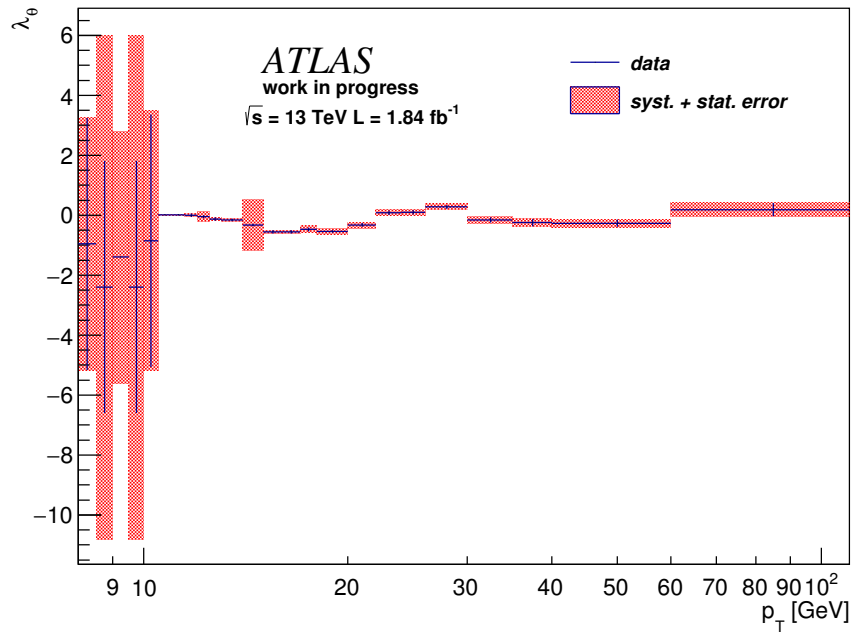


Figure 5.4: Fit result for λ_ϕ as a function of J/ψ p_T .

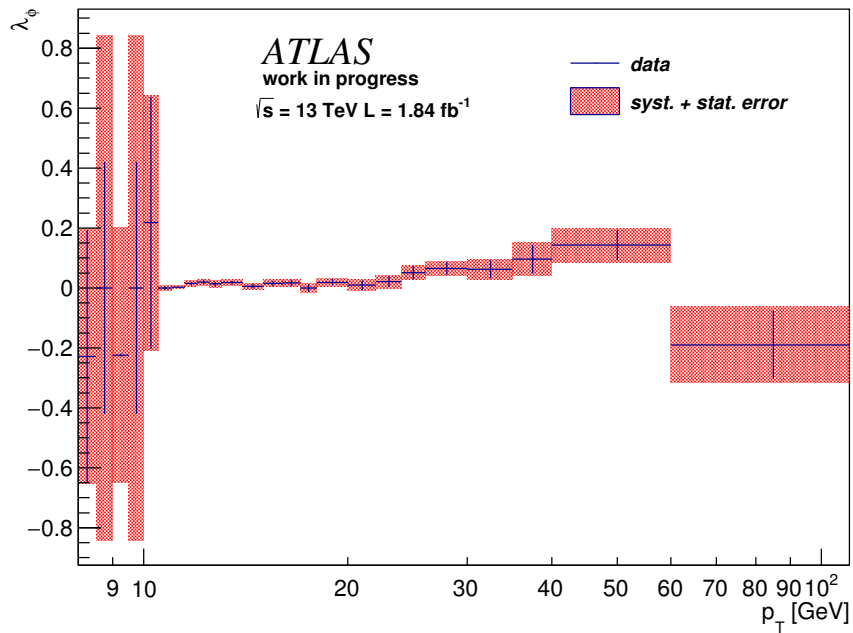


Figure 5.5: Fit result for λ_ϕ as a function of J/ψ p_T .

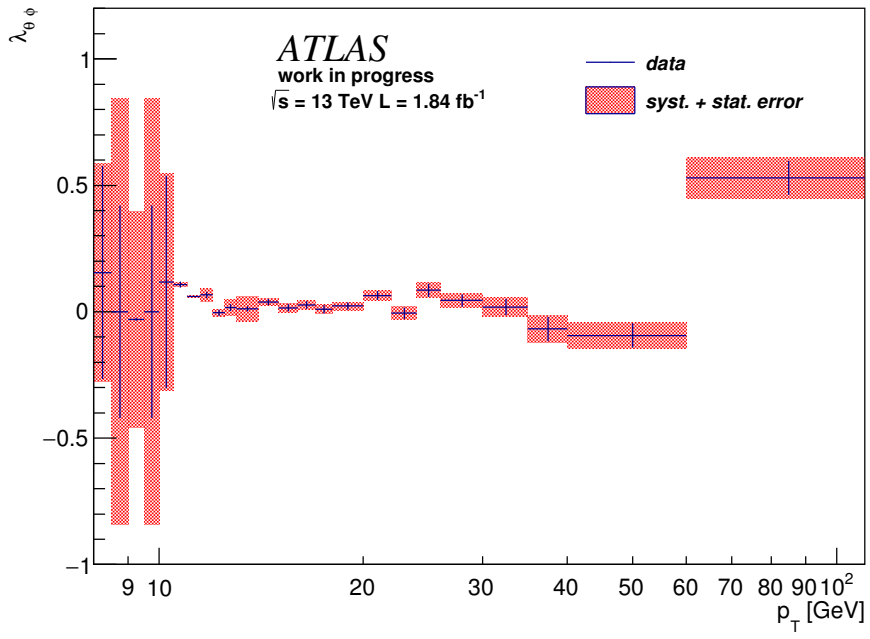


Figure 5.6: Fit result for $\lambda_{\theta\phi}$ as a function of J/ψ p_T .

Chapter 6

Conclusions

The first measurement of J/ψ polarization at $\sqrt{s} = 13$ TeV in proton-proton collisions using ATLAS detector is presented in this thesis. The analysis is based on the $J/\psi \rightarrow \mu^+\mu^-$ decay channel and it uses data sample with integrated luminosity 1.84 fb^{-1} .

In order to select only prompt J/ψ , produced in the primary vertex, and subtract the non-prompt produced J/ψ , from a decay of B-hadrons, and background, the simultaneous unbinned mass-lifetime fit is performed. Using the result of the fit, the non-prompt fraction and cross section of prompt J/ψ is measured. The non-prompt contribution rises from approximately 25% at p_T of 8 GeV up to 70% at p_T of 100 GeV. The results corresponds to the previous measurement at $\sqrt{s} = 8$ TeV and demonstrate the correctness of the selection criteria and offsetting detector effects.

After the unbinned mass-lifetime fit and cut on J/ψ invariant mass, the non-prompt and background contributions are reduced under 20%. Performing the subtraction of the sideband events from signal region, the high purity prompt J/ψ data sample is obtained. For each p_T bin, the Monte Carlo template is produced and the final polarization template fit can be performed.

The polarization parameters are obtained in helicity frame as a function of J/ψ p_T and from the preliminary results it shows, that the prompt J/ψ have zero polarization. The polarization MC template fit has difficulties to converge in the low p_T region under 11 GeV. The obtained results are in agreement with previous measurement at the CMS and the LHCb, but in clear disagreement with NLO NRQCD calculations which were the most prominent to describe the heavy quarkonia production mechanism. The measurement is still work in progress and uses preliminary efficiency maps, therefore the result is not finished and complete and the final polarization can significantly change.

In the future, the systematic uncertainties originating from efficiency maps and fitting models need to be computed and included in the result. Furthermore, the stability of polarization MC template fitting procedure needs to be improved. The MC samples used to produce fitting templates suffer from insufficient statistics in the high p_T region and to correct that, the MC data sample with higher p_T threshold on single muon or significantly more events need to be generated.

Bibliography

- [1] Burton Richter. Nobel Lecture: From the Psi to Charm – The Experiments of 1975 and 1976. http://www.nobelprize.org/nobel_prizes/physics/laureates/1976/richter-lecture.html. Accessed: 2014-05-21.
- [2] Samuel Chao Chung Ting. Nobel Lecture: The Discovery of the J Particle: A Personal Recollection. http://www.nobelprize.org/nobel_prizes/physics/laureates/1976/ting-lecture.html. Accessed: 2014-05-21.
- [3] J. Beringer et al. (Particle Data Group), Phys. Rev. D86, 010001 (2012) and 2013 partial update for the 2014 edition.
- [4] Evidence for the spin-0 nature of the higgs boson using {ATLAS} data. *Physics Letters B*, 726(1–3):120 – 144, 2013.
- [5] Donald H. Perkins. *Introduction to high energy physics*, volume 2. Addison-Wesley Reading, Massachusetts, 1987.
- [6] Elena Giusarma, Roland de Putter, Shirley Ho, and Olga Mena. Constraints on neutrino masses from Planck and Galaxy Clustering data. *Phys.Rev.*, D88(6):063515, 2013.
- [7] Ubaldo Dore and Lucia Zanello. Bruno Pontecorvo and neutrino physics. 2009.
- [8] Y. et al. Fukuda. Evidence for oscillation of atmospheric neutrinos. *Phys. Rev. Lett.*, 81:1562–1567, Aug 1998.
- [9] Felix Siebenhühner. Determination of the qcd coupling constant from charmonium. <http://theorie.ikp.physik.tu-darmstadt.de/nhc/pages/lectures/rhiseminar07-08/siebenhuehner.pdf>. Accessed: 2014-05-21.
- [10] Taichi Kawanai and Shoichi Sasaki. Heavy quarkonium potential from Bethe-Salpeter wave function on the lattice. *Phys.Rev.*, D89:054507, 2014.
- [11] Hiroki Sato. J/ψ production in $p+p$ collisions at $\sqrt{s} = 200$ GeV. *Mem. Fac. Sci. Kyoto (Ser. A Phys. Astrophys. Geophys. Chem.)*, 44:89–193, 2003.

- [12] Pietro Faccioli, Carlos Lourenco, Joao Seixas, and Hermine K. Wohri. Towards the experimental clarification of quarkonium polarization. *Eur. Phys. J.*, C69:657–673, 2010.
- [13] Pietro Faccioli, Carlos Lourenço, and João Seixas. New approach to quarkonium polarization studies. *Phys. Rev. D*, 81:111502, Jun 2010.
- [14] John C. Collins and Davison E. Soper. Angular distribution of dileptons in high-energy hadron collisions. *Phys. Rev. D*, 16:2219–2225, Oct 1977.
- [15] Eric Braaten, Daekyoung Kang, Jungil Lee, and Chaehyun Yu. Optimal spin-quantization axes for the polarization of dileptons with large transverse momentum. *Phys. Rev. D*, 79:014025, Jan 2009.
- [16] K. Gottfried and J. D. Jackson. On the connection between production mechanism and decay of resonances at high energies. *Il Nuovo Cimento (1955-1965)*, 33(2):309–330, 2007.
- [17] Bryan Fulson. Quarkonia production and polarization at the hadron colliders. In *Proceedings, 2nd Conference on Large Hadron Collider Physics Conference (LHCP 2014)*, 2014.
- [18] Geoffrey T. Bodwin, Eric Braaten, and Jungil Lee. Comparison of the color-evaporation model and the NRQCD factorization approach in charmonium production. *Phys. Rev.*, D72:014004, 2005.
- [19] John C. Collins, Davison E. Soper, and George F. Sterman. Factorization of Hard Processes in QCD. *Adv. Ser. Direct. High Energy Phys.*, 5:1–91, 1989.
- [20] R. Baier, R. Rückl. Hadronic collisions: A quarkonium factory. *Z. Phys. C - Particles and Fields*, 19(3):251–266, 1983.
- [21] H. Fritzsche and K.-H. Streng. Quarkonium decay into heavy quark flavours. *Physics Letters B*, 77(3):299 – 303, 1978.
- [22] Gouranga C. Nayak. Proof of NRQCD Factorization at All Order in Coupling Constant in Heavy Quarkonium Production. 2015.
- [23] M. G. Ryskin, Yu. M. Shabelski, and A. G. Shuvaev. Heavy quark production in hadron collisions. In *34th Annual Winter School on Nuclear and Particle Physics (PNPI 2000) Gatchina, Russia, February 14-20, 2000*, 2000.
- [24] Monica Pepe Altarelli. Quarkonium Production at LHCb. *EPJ Web Conf.*, 60:15005, 2013.
- [25] Edward H. Thorndike. Bottom quark physics: Past, present, future. In *Probing luminous and dark matter. Proceedings, Symposium in Honor of Adrian Melissinos, Rochester, USA, September 24-25, 1999*, pages 127–159, 1999.

- [26] Natalia Panikashvili. The {ATLAS} b-physics program. *Nuclear Physics B - Proceedings Supplements*, 185:201 – 206, 2008. Proceedings of the Second Workshop on Theory, Phenomenology and Experiments in Heavy Flavour Physics.
- [27] Giulia Tellarini. Measurements of $b \rightarrow b$ and $b \rightarrow s$ mixing frequencies at lhcb. *Journal of Physics: Conference Series*, 556(1):012038, 2014.
- [28] Accelerators and Technology Sector. The CERN accelerator complex . <https://espace.cern.ch/acc-tec-sector/default.aspx>. Accessed: 2014-05-12.
- [29] CERN. The accelerator complex. <http://home.web.cern.ch/about/accelerators>. Accessed: 2014-05-12.
- [30] R. Bruce, G. Arduini, S. Fartoukh, M. Giovannozzi, M. Lamont, E. Metral, T. Pieloni, S. Redaelli, and J. Wenninger. Baseline LHC machine parameters and configuration of the 2015 proton run. In *Proceedings, LHC Performance Workshop (Chamonix 2014)*, pages 100–106, 2015.
- [31] Marco Battaglia. Status and Expectations from LHC Run 2. <https://indico.cern.ch/event/307465/contributions/1675934/attachments/586320/807017/CERNWinterSchool2015.pdf>. Accessed: 2016-04-30.
- [32] CERN Administrative Information Services. Experiments at CERN. <http://greybook.cern.ch/>. Accessed: 2014-04-08.
- [33] The ATLAS Collaboration et al. . The atlas experiment at the cern large hadron collider. *Journal of Instrumentation*, 3(08):S08003, 2008.
- [34] A. Yamamoto, Y. Makida, R. Ruber, Y. Doi, T. Haruyama, F. Haug, H. ten Kate, M. Kawai, T. Kondo, Y. Kondo, J. Metselaar, S. Mizumaki, G. Olesen, O. Pavlov, S. Ravat, E. Sbrissa, K. Tanaka, T. Taylor, and H. Yamaoka. The {ATLAS} central solenoid. *Nuclear Instruments and Methods in Physics Research Section A: Accelerators, Spectrometers, Detectors and Associated Equipment*, 584(1):53 – 74, 2008.
- [35] Zlobin, A. V. 2014. Superconducting Magnets - Principles, Operation, and Applications. Wiley Encyclopedia of Electrical and Electronics Engineering. 1–19.
- [36] M Aleksa, F Bergsma, P A Giudici, A Kehrl, M Losasso, X Pons, H Sandaker, P S Miyagawa, S W Snow, J C Hart, and L Chevalier. Measurement of the atlas solenoid magnetic field. *Journal of Instrumentation*, 3(04):P04003, 2008.
- [37] Track Reconstruction Performance of the ATLAS Inner Detector at $\sqrt{s} = 13$ TeV. Technical Report ATL-PHYS-PUB-2015-018, CERN, Geneva, Jul 2015.
- [38] Sara Valentineti. *Luminosity measurements with the LUCID detector in the ATLAS experiment*. PhD thesis, Bologne U., 2011.

- [39] The ATLAS luminosity measurement taskforce . <http://lunvis.web.cern.ch/lunvis/taskforce/main.html>. Accessed: 2016-05-03.
- [40] *2013 IEEE Nuclear Science Symposium and Medical Imaging Conference (2013 NSS/MIC)*, 2013.
- [41] Georges Aad et al. Measurement of the total cross section from elastic scattering in pp collisions at $\sqrt{s} = 7$ TeV with the ATLAS detector. *Nucl. Phys.*, B889:486–548, 2014.
- [42] ATLAS Luminosity Public Results Run 2. <https://twiki.cern.ch/twiki/bin/view/AtlasPublic/LuminosityPublicResultsRun2>. Accessed: 2016-05-03.
- [43] ATLAS Luminosity Calculator. <https://atlas-lumicalc.cern.ch/>. Accessed: 2016-05-03.
- [44] Yu Nakahama. The atlas trigger system: Ready for run-2. *Journal of Physics: Conference Series*, 664(8):082037, 2015.
- [45] Trigger Operation Public Results. <https://twiki.cern.ch/twiki/bin/view/AtlasPublic/TriggerOperationPublicResults>. Accessed: 2016-05-03.
- [46] 2015 start-up trigger menu and initial performance assessment of the ATLAS trigger using Run-2 data. Technical Report ATL-DAQ-PUB-2016-001, CERN, Geneva, Mar 2016.
- [47] B Physics Trigger Public Results. <https://twiki.cern.ch/twiki/bin/view/AtlasPublic/BPhysicsTriggerPublicResults>. Accessed: 2016-05-03.
- [48] Rene Brun and Fons Rademakers. An Object Oriented Data Analysis Framework. <ftp://root.cern.ch/root/lausanne.ps.gz>. Accessed: 2014-05-21.
- [49] The ROOT Team. RooFit. <http://root.cern.ch/drupal/content/roofit>. Accessed: 2014-05-18.
- [50] Athena The ATLAS Common Framework . <http://atlas-computing.web.cern.ch/atlas-computing/documentation/swDoc/AthenaDeveloperGuide-8.0.0-draft.pdf>. Accessed: 2016-05-03.
- [51] Torbjorn Sjostrand, Stephen Mrenna, and Peter Z. Skands. A Brief Introduction to PYTHIA 8.1. *Comput. Phys. Commun.*, 178:852–867, 2008.
- [52] S. Agostinelli et al. Geant4—a simulation toolkit. *Nuclear Instruments and Methods in Physics Research Section A: Accelerators, Spectrometers, Detectors and Associated Equipment*, 506(3):250 – 303, 2003.
- [53] Steven FARRELL, David Adams, Paolo Calafiura, Pierre-Antoine Delsart, Markus Elsing, Karsten Koeneke, Attila Krasznahorkay, Nils Krumnack, Eric Lancon, Wim Lavrijsen, Paul Laycock, Xiaowen Lei, Sara Kristina Strandberg, Wouter Verkerke, Iacopo Vivarelli, and

- Martin Woudstra. Dual-use tools and systematics-aware analysis workflows in the ATLAS Run-2 analysis model. Technical Report ATL-SOFT-PROC-2015-019. 3, CERN, Geneva, May 2015.
- [54] Georges Aad et al. Measurement of the muon reconstruction performance of the ATLAS detector using 2011 and 2012 LHC proton–proton collision data. *Eur. Phys. J.*, C74(11):3130, 2014.
- [55] S. Hassani, L. Chevalier, E. Lancon, J. F. Laporte, R. Nicolaidou, and A. Ouraou. A muon identification and combined reconstruction procedure for the ATLAS detector at the LHC using the (MUONBOY, STACO, MuTag) reconstruction packages. *Nucl. Instrum. Meth.*, A572:77–79, 2007.
- [56] Georges Aad et al. Measurement of the differential cross-sections of prompt and non-prompt production of J/ψ and $\psi(2S)$ in pp collisions at $\sqrt{s} = 7$ and 8 TeV with the ATLAS detector. 2015.
- [57] Measuring Electron Efficiencies at CMS with Early Data. Technical Report CMS-PAS-EGM-07-001, CERN, 2008. Geneva, Dec 2008.
- [58] Internal communication.
- [59] Tomasz Skwarnicki. A study of the radiative cascade transitions between the upsilon-prime and upsilon resonances. DESY-F31-86-02.